TECHNISCHE UNIVERSITÄT WIEN
Vienna | Austria

DIPLOMARBEIT

Optical coherence tomography for vascular skin imaging

Ausgeführt am
Institut für Angewandte Physik
Technische Universität Wien

unter der Anleitung von
Ao. Univ.-Prof. DI Dr. Martin Gröschl

in Zusammenarbeit mit
Assoc. Prof. DI Dr. Michael Pircher

am
Zentrum für Medizinische Physik und Biomedizinische Technik
Medizinische Universität Wien

durch
Martin E. Fürst
Wigandgasse 18, 3400 Klosterneuburg

February 9, 2017

Acknowledgements

I want to thank Prof. Gröschl for his straightforwardness in organising and supervising this thesis. He was always quick to reply and uncomplicated in all issues that came up.

The main workload of scientific supervision was carried out by Dr. Michael Pircher. I want to express my profound gratitude for his kindness, his patience and his good humour throughout the last year. Without him, this thesis could not exist and I am grateful for having had the chance to take part in such a recent and important field of study.

Last but not the least, I would like to thank my family: my parents and my sisters, for continuous encouragement throughout my years of study and finally the writing of this thesis.

Abstract

Optical coherence tomography is a non-invasive, optical imaging technique. It is based on low-coherence interferometry. Main applications can be found in medicine, due to its relatively high penetration depth in tissue ($1 - 3\,\mathrm{mm}$) and an axial resolution in the µm-range. OCT systems can be categorized into Time-Domain and Spectral-Domain systems. Especially the latter are becoming increasingly important.

Goal of the presented thesis was the optimization of an existing Spectral-Domain-OCT system to enable in-vivo imaging of capillaries in the human nailfold. The novel aspect is that both, the amplitude and the phase information provided by the OCT system, is used to generate vascular maps of tissue. Corresponding evaluation software was developed in the programming language LabView. The system was characterized and tested on various skin regions. Specific focus of this work was set to the reproducibility of measurements of the vascular network in the nailfold.

Zusammenfassung

Die optische Kohärenztomographie (OCT von engl. Optical Coherence Tomography) ist ein nicht-invasives, bildgebendes Verfahren und basiert auf der Weißlicht-Interferometrie.

Durch die relativ hohe Eindringtiefe in biologisches Gewebe ($1 - 3\,\mathrm{mm}$) und axiale Auflsung im µm-Bereich findet die Technik vor allem in der Medizin Anwendung. Es lassen sich zwei Arten von OCT-Systemen unterscheiden: Time-Domain (TD-OCT) und Spectral-Domain (SD-OCT), wobei vor allem letztgenannte immer weiter verbreitet werden.

Das Ziel der präsentierten Arbeit war es, ein bestehendes SD-OCT-System zu optimieren um die Kapillaren der menschlichen Nagelfalz in-vivo darstellen zu können. Erstmals sollen dabei sowohl die Amplituden- als auch die Phaseninformation benutzt werden. Zu diesem Zweck wurde eine entsprechende Analyse-Software in LabView erstellt. Das OCT-System wurde an verschiedenen Hautstellen getestet und charakterisiert. Besonderes Augenmerk wurde auf die Reproduzierbarkeit von Messungen des Gefäßnetzwerks in der Nagelfalz gelegt.

Contents

Chapter 1

Introduction

The interest in capillaries close to the nailfold started in 1663, when Johan Kolhaus was the first clinician to observe them ([1]). About a hundred years later, Giovanni Rasori discovered a close relationship between conjunctival inflammation and changes in the capillary pattern. In 1862, Maurice Raynaud presented his thesis on ischaemic damage of the hands, feet and nose. In the course of that thesis, he established capillaroscopy as an important diagnostic tool for the aforementioned pathologies now known as Raynaud's phenomenon ([1]).

In the twentieth century, capillaroscopy is an established technique to distinguish between two forms of Raynaud's phenomenon (RP): Primary RP and secondary RP, which is a symptom of systemic sclerosis - an autoimmune disease.

Interest in cutaneous microcirculation arises also from its potential use as an indicator of diseases such as Diabetes Mellitus ([2]). Assessment of microcirculation might also be of use in intensive care units, as studies showed a decrease in sublingual capillary density in patients with acute sepsis ([3]). Common techniques for the visualization of human microcirculation are ([3]):

- Standard light microscope: The use of lenses and microscopes to study anatomical details dates back centuries. A documented case of a light microscope used to study skin microvascularity is Gilje 1953 ([4]).

- Video capillaroscopy: Combining a microscope with a videocamera allows the study of flow velocities and storage of data for retrospective analysis. Systems like that can be traced back to the 1970s ([5]).

- Fluorescence videomicroscopy: In the 1980s, Bollinger et. al. ([6]) introduced fluorescent tracers such as Na-fluorescein and indocyanine green to the above-mentioned systems. When combined with appropriate filters, these tracers greatly enhance the image contrast, rendering the technique fit for study of Raynaud's phenomenon ([7]).

- Orthogonal polarization spectral imaging: A different approach to increase image contrast is the use of green light, which is absorbed by haemoglobin, making red blood cells to appear dark ([8]). This technique is limited to skin regions with a very thin epidermal layer.

- Hand-held video-capillaroscopy setups: Since the 2000s, due to industrial uses, digital videomicroscopes have become smaller and cheaper. These modern, hand-held systems can easily be used in combination with digitalization systems for post-processing and data-storage ([9]).

All these techniques are based on classic, optical microscopy. An entirely different approach is the use of optical coherence tomography to perform capillaroscopy. Optical coherence tomography or OCT is an optical imaging technique based on white-light interferometry.

Very briefly, its history can be sketched as follows ([10]). Starting 1971, with the "light in flight" experiments of Michel Duguay, which was a femtosecond optics experiment employing an ultrafast shutter. Duguay proposed that through selective time gating, it should be possible to "see inside" biological structures. In the 1980s, Erich Ippen at MIT used the concept of nonlinear cross correlation to "gate out" unwanted scattered light and measure the length of an ex-vivo bovine eye. Around the same time, research groups suspected that it might be possible to measure light echoes using interferometry and in 1988, Fercher et. al. used low-coherence interferometry to measure axial eye length ([11]). David Huang continued research on low-coherence interferometry and published the first image of multiple gray-scale A-scans combined to form a two-dimensional image or B-scan ([12]). In 1993, the first in-vivo images of the retina were acquired using time-domain OCT systems ([13]). At about the same time, companies started to show interest and 1996 the first commercial opthalmic OCT device entered the market. In 2003, the sensitivity advantage of Fourier-Domain systems over time-domain systems was demonstrated ([14]). Since then, OCT has become a standard of care in opthalmology, with cumulative procedures passing 100 million (worldwide) in 2010.

In this thesis, OCT-imaging on human skin was used to visualize the capillary network. This is sometimes referred to as OCT-angiography (OCT-A) and is supposed to have several advantages compared to classic capillaroscopy. OCT offers a high image contrast, possibly allowing for more automated vessel detection. As OCT records volumetric data sets, the vessels can also be discriminated by their depth in the tissue, which is currently not achieved in microscopy. The feasibility of this approach has already been demonstrated (see e.g. [2], [15], [16]). The aim of this thesis was to test the reproducibility of the acquired vessel maps and install a system fit for further use.

Chapter 2 will introduce the theoretical basis of OCT. Especially Fourier-Domain-OCT and its sensitivity will be discussed.

In chapter 3, the setup used for this thesis is presented. Both the hardware and the software will be introduced.

Chapter 4 gives the experimental results of this thesis. Starting with the characterization of the system (spectrometer efficiency, signal-to-noise-ratio, field of view), the main emphasis is on *in-vivo* imaging of microcirculation of human skin.

Finally, results are discussed in chapter 5 and an outlook is given on possible future extensions of the system.

Chapter 2

Theoretical Background

2.1 Imaging Capillaries of the nailfold

This section was also presented in a project work prior to this thesis ([17]).

Microcirculation is necessary for life and function of all organs in the human body([3]). The single cell needs to be supplied with oxygen and nutrients. At the same time, the cell also needs to release waste products and carbondioxide. Capillary vessels take care of these two tasks. Local failure of the microcirculation can result in necrosis (cell death), while systemic failure (as in shock) can result in death of the whole organism ([3]).

The microcirculatory network is made up of arterioles, capillaries and venules. The exact arrangement of these varies among different tissues. In hand and feet, the microvessels can be divided in a network responsible for nutritive tasks and a network mainly for thermoregulatory functions ([3]). The superficial capillaries lie perpendicular to the skin surface in most locations. Therefore, they are only visible as dots or comma-shaped apexes in *in-vivo* microscopy. The nailfold is a region where the capillaries lie parallel to the surface and therefore appear U-shaped in microscopy and resemble hairpins. This is the main motivation for imaging the capillaries in the nailfold. The drawing shown in figure 2.1 shows the characteristic shapes of healthy and pathological capillaries.

2.2 Low-Coherence Interferometry

OCT has its origins in low-coherence interferometry (LCI), which is a non-contact optical sensing technology usually employing a Michelson-Interferometer and a light source with relatively low coherence length ([19], [20]). LCI was invented for characterization of optoelectronic components and can be used for absolute measurements of depths of surface boundaries or thicknesses of layers. Light from one arm of the interferometer is directed at a sample consisting of multiple semi-transparent layers and light from the other arm is reflected by a moveable mirror. Reflections occurr at boundaries between layers with different refractive indices. When using a light source with limited coherence length, only light that travelled the

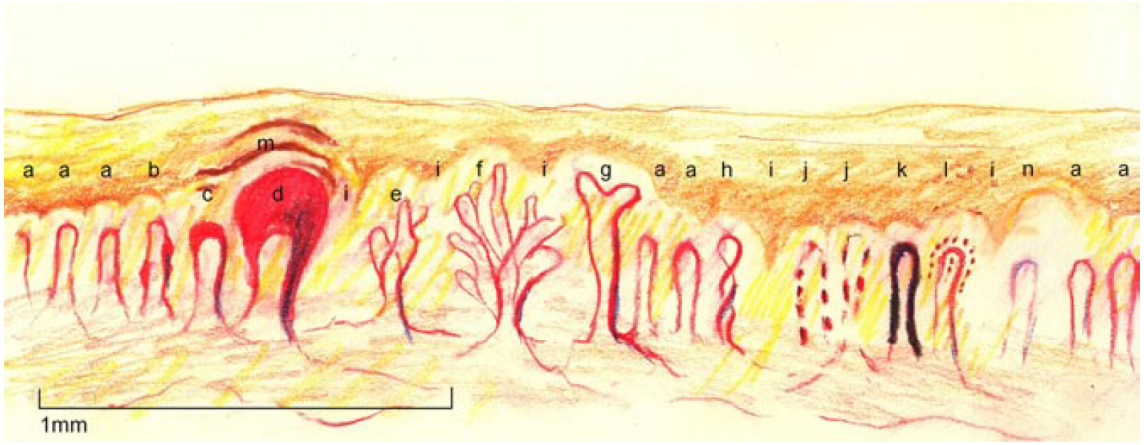

Figure 2.1: Characteristic appearances of nailfold capillaries: a) Healthy subject, b) diameter changes, c) ectasia, d) giant capillary, e) branching, f) cluster capillaries, g) elongation, h) torsion, i) rarefaction, j) sludge, k) thrombosis, l) microbleeding, m) hemmorhage, n) edema (Figure taken from [18], with permission by Springer, license number 3891400709419)

same distance (is reflected from a depth in the sample corresponding to the position of the reference arm mirror) can interfere with light from the reference arm (see figure 2.2).

To scan the depth of the sample, the reference mirror needs to be shifted while the interference pattern or photocurrent is detected. This is typically done with a constant velocity v. The optical path difference between the two interferometer arms therefore increases with $\Delta s = 2vt$. The detected raw signal has the shape of an amplitude-modulated cosine-function with frequency $f = 2v/\lambda_0$ (with λ_0 being the central wavelength of the light). Modulation maxima appear whenever the mirror position corresponds to a highly reflective layer in the sample. These maxima become more narrow (and allow distinction of thinner layers) with smaller coherence length of the used light. The coherence length l_c is of the order $l_c \approx \lambda_0^2/\Delta\lambda$ (with $\Delta\lambda$ as the spectral bandwidth of the light). As the axial resolution directly results from the broadness of the modulation maxima, it improves with higher spectral bandwidth.

2.2.1 Coherence length, axial resolution and imaging depth

Stationary interference patterns can only be observed when the phase difference $\Delta\phi$ between any superposing waves changes by less than 2π during the observation time. There's a number of possible reasons for a change in phase difference ([21]):

- The central frequency of the light source changes with time.
- The source emits wave trains of limited length with statistically distributed phases.
- The refractive index of the medium between source and observer varies with time.

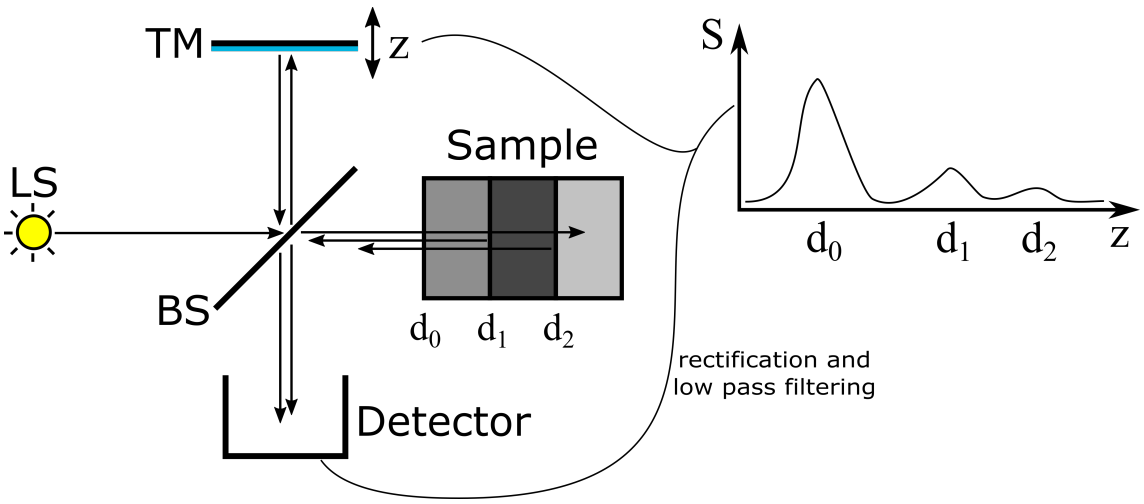

Figure 2.2: Principle of low-coherence interferometry. Light from the light source (LS) travels to a beam splitter BS. The light is split into sample and reference beam, respectively. Part of the light is reflected by a moveable mirror TM (the reference mirror). The other part shines upon the sample. Boundary surfaces within the sample reflect part of the incident light. Light waves returning from the reference and the sample arm recombine and interfere at the beamsplitter and the intensity is detected by a detector at the interferometer exit. Relating the position z of the reference mirror to the intensity of the interference signal S gives a curve as shown in the right half of the figure. From the position of the signal peaks, the depth of the reflecting layer can be calculated (if the refractive indices of the layers are known).

In absence of limiting influences as listed above, the spectral bandwidth $\Delta\nu$ of the source limits the time light may travel before violating the requirement formulated above. Considering only the partial waves with the highest (ν_2) and lowest (ν_1) frequency within $\Delta\nu$, the phase difference between these two at time t can be calculated as

$$\Delta\phi(t) = 2\pi(\nu_2 - \nu_1)t \tag{2.1}$$

It can immediately be seen that after $t = \frac{1}{\nu_2 - \nu_1} = \frac{1}{\Delta\nu}$, $\Delta\phi$ equals 2π. This maximum time $\tau_c = 1/\Delta\nu$ is referred to as the *coherence time*.

The distance light can travel during the coherence time is called the coherence length $l_c = c \cdot \tau_c$. This can also be re-written as a function of wavelength λ instead of frequency ν, yielding

$$l_c = c \cdot \frac{\lambda_0^2 - \Delta\lambda^2}{c \cdot \Delta\lambda} = \frac{\lambda_0^2 - \Delta\lambda^2}{\Delta\lambda} \approx \frac{\lambda_0^2}{\Delta\lambda} \tag{2.2}$$

Taking into account the typical Gaussian shape of frequency profiles, a more refined formula can be written (see [20]):

$$l_c = \frac{4\ln(2)\lambda_0^2}{\pi \cdot \Delta\lambda} \tag{2.3}$$

Low Coherence Interferometry measures the depth of a reflecting layer by displacing the reference mirror of a Michelson-Interferometer and recording of the interference signal. For light with low coherence length, an interference signal can only be detected when the depth closely matches the mirror displacement. Smaller coherence lengths allow for more precise depth measurements. Therefore, the depth resolution of an LCI system is limited by the bandwidth of the lightsource and equals half of the coherence length given in the equation 2.3. The factor 1/2 results from the roundtrip of light within the Michelson-Interferometer.

Optical coherence tomography employs the same principle to obtain 3D information from a sample. Typically, this is achieved by equipping the system with two scanning means: One to scan the object in depth and one to scan the object transversally. The use of sensor arrays, charged coupled device (CCD) cameras or arrays of emitters can eliminate the need for scanning.

Modern OCT systems that are used in the field of medicine are operated at wavelengths in the $800 - 1300\,\text{nm}$ range and achieve axial resolutions of a few micrometers ([20]).

2.3 Fourier-Domain OCT (FD-OCT)

The imaging principles of Low-Coherence-Interferometry directly translate to so-called Time-Domain-OCT, which were the earliest systems put to clinical and biological use ([22]). However, the need to scan 10 ps delays at kilohertz rates requires relatively complicated optical and mechanical designs ([22]). An alternative method to this coherence-gating involves recording of the interferometric signal as a function of optical wavenumber. This so-called *Fourier-Domain* or FD-OCT approach is taken by

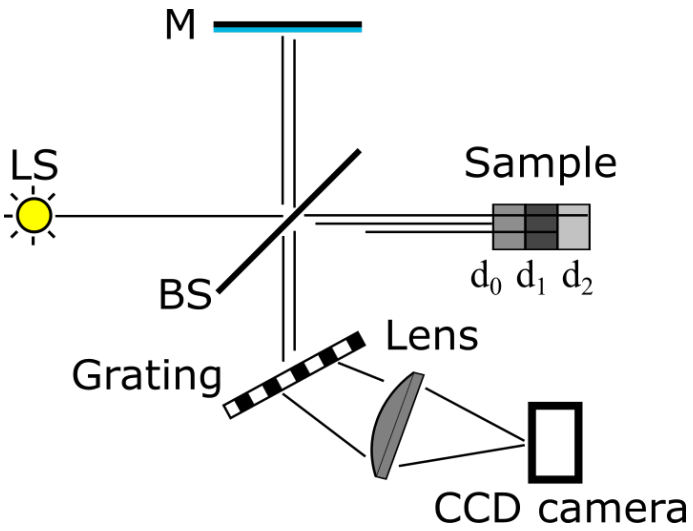

Figure 2.3: A possible Fourier-Domain-OCT setup. It is very similar to the free-beam LCI-setup shown in figure 2.2. The moveable mirror is replaced by a stable mirror M and instead of a simple single detector, a spectrometer and a CCD camera are used. In this case, the spectrometer consists of a lens, a transmission grating and a line-scan camera.

two distinct methods: The Spectral-Domain-OCT (SD-OCT) and the Swept-Source-OCT (SS-OCT). In the SD-OCT case, a broadband light-source and a dispersive spectrometer in the detection arm are used. Swept-Source-systems employ a narrow-band light-source that is rapidly tuned through a broad bandwidth. It was shown ([22]), that FD-OCT techniques have a generally higher sensitivity than TD-OCT systems.

For this thesis, a Spectral-Domain-OCT-system was used. Its theoretical basis will therefore be introduced here.

2.3.1 Spectral-Domain-OCT

In Spectral-Domain OCT, information about the axial structure of the sample is obtained through the use of a broadband light source and a spectrometer. In figure 2.3, a Spectral-Domain-OCT setup with a spectrometer consisting of a lens, a transmission grating and a line-scan camera is sketched. Note the similarity to the LCI-setup, but that the moving mirror is now replaced by a stable mirror. SD-OCT is attractive because it eliminates the need for depth scanning as in time domain OCT, where this is typically achieved by mechanical means ([20]). In addition, the light returning from the entire sample depth contributes to the interference pattern which yields a much higher sensitivity compared to the TD-OCT approach.

When using a broadband source in a Michelson-Interferometer, the spectrum of the interference signal shows a modulation depending on the optical pathway difference between the two arms. In an OCT-setup, a partially reflecting sample is placed in one interferometer arm and *each* reflecting layer of the sample imprints a modulation on the spectrum. The frequency of such a modulation corresponds to the depth of the layer and their magnitude to the reflectivity. When a spectrometer

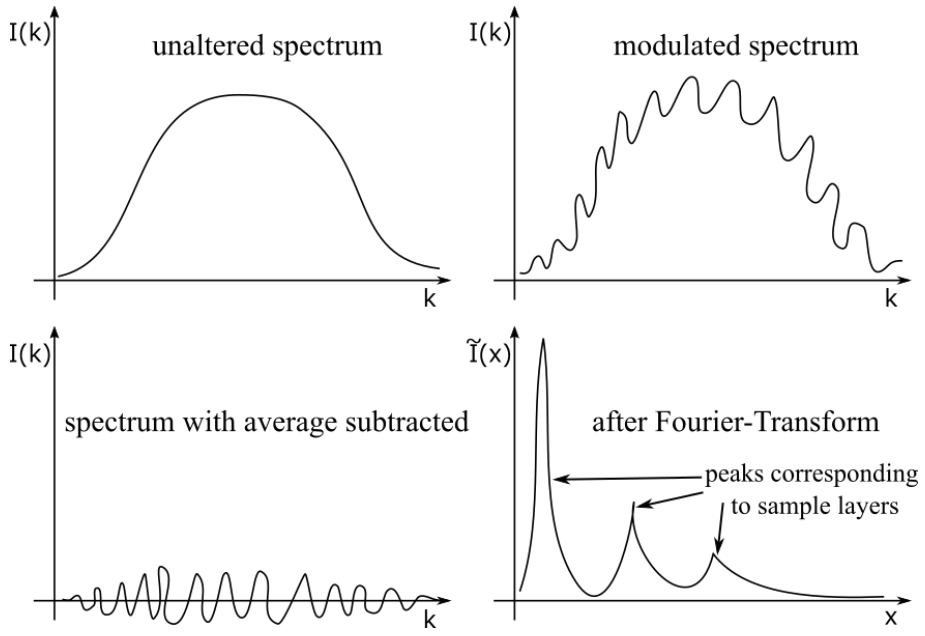

Figure 2.4: A rough representation of the Fourier-Domain principle. The "unaltered spectrum" is the spectrum of the light source. Because of interference of light components returning from sample and reference arm, a modulated spectrum can be observed. The modulation frequency depends on the path length difference of the light. Larger difference results in higher frequencies. Subtracting the original spectrum leaves only the modulations, which are represented as peaks in the Fourier-transformed spectrum.

and a CCD camera are used, the spectrum can be recorded and transformed into an electrical signal. Fourier-transforming this spectrum translates the periodicity of the modulations into peaks at different frequencies, related to the optical path differences. This principle is illustrated in figure 2.4.

In this fashion, a complete depth-profile, or *A-scan*, can be obtained from a single interference signal. Scanning means in the sample arm are still necessary to obtain a volumetric data set.

SNR in FD-OCT

As CCD detectors collect photoelectron charges during the complete exposure time τ, SD-OCT setups measure optical *energy*, not *power* (which is what the PIN-diodes used in TD-OCT systems measure) ([14]). The number of photoelectrons n_e is related to the optical power P as (with h being the Planck constant, ν_0 the light frequency and η the detector efficiency):

$$n_e = \eta P \tau / h\nu_0 \tag{2.4}$$

Following [14], with ρ, γ_r, γ_s, R_r and R_s denoting the losses in the spectrometer, reference arm, sample arm and the respective mirrors, the signal in the FD-OCT system can be written as

$$S(\tau)_{Peak} = \frac{\rho\eta\tau P_0}{h\nu_0 N}\sqrt{\gamma_r\gamma_s R_r R_s} \tag{2.5}$$

The unfavorable $1/N$ factor is compensated because overall noise after Fourier-Transformation is

$$\tilde{\sigma}^2_{noise} = \frac{1}{N}\sigma^2_{noise} = \frac{1}{N}(\sigma^2_{shot} + \sigma^2_{excess} + \sigma^2_{receiver}) \tag{2.6}$$

and sensitivity S in SD-OCT is defined as:

$$S = \langle S^2 \rangle / \tilde{\sigma}^2_{noise} \tag{2.7}$$

Shot-noise is given as:

$$\sigma^2_{shot} = \frac{\rho\eta\tau P_0}{h\nu_0 N}(\gamma_s R_s + \gamma_r R_r) \tag{2.8}$$

Assuming shot-noise limited detection and $R_s << R_r$, the signal-to-noise ratio can be written as (see also [23] for a different derivation, P_{sample} is the power of the light in the sample arm):

$$S = \frac{\eta\rho P_{sample}\tau}{h\nu} \tag{2.9}$$

2.3.2 OCT terminology (A, B, C scan)

Depending on the type and exact variant of an OCT system, different scanning protocols are possible. However, in all cases a single-line depth profile is referred to as an *A-scan* ([20]. A *B-scan* can be generated by collecting many A-scans from adjacent positions (see figure 2.5a). The B-scan is a two-dimensional cross section of the object. When the OCT system is equipped with a depth-scanning mechanism (such as in a Time-Domain system), it is possible to scan the sample transversely at a fixed depth. A line-scan of this type is referred to as a *T-scan* (see figure 2.5b). If the system allows for T-scans, B-scans can be obtained by collecting multiple T-scans from adjacent positions along a longitudinal axis. In this case, the B-scan is also a cross-section along the depth of the sample.

An *upfront* cross-section, or "en-face" image of the object is called a *C-scan*. This can either be obtained by collecting T-scans from positions adjacent to each other along an axis orthogonal to the incident light beam or calculated from the volumetric dataset.

2.4 Detecting movement in OCT images

Axial resolution increases with decreased coherence length (refer to chapter 2.2) and coherence length decreases with the wavelength. Low wavelengths therefore seem desirable. But on the other hand, the penetration depth of light into biological tissue is highest in the *near-infrared window* in the range of $650 - 1350\,\text{nm}$. Thus, it is comon in OCT for skin imaging to use light in the 1300 nm wavelength region. The basic problem in OCT for detecting vasculature is, that there is little absorption contrast of infrared light between vessel tissue and the surrounding tissue. Therefore, to detect vessels *in-vivo* with an OCT system, multiple measurements, that are separated in time, are performed.

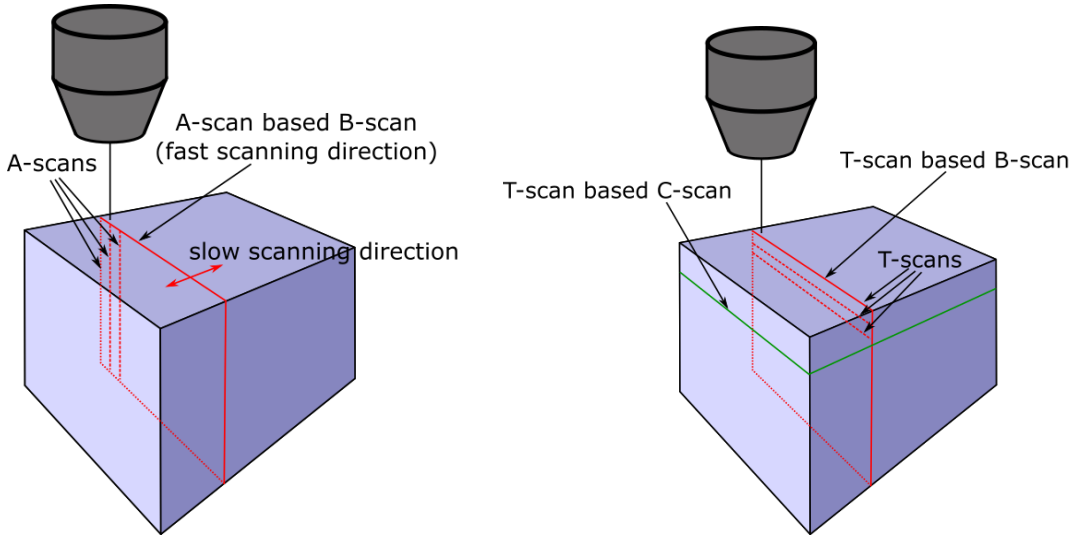

(a) (b)

Figure 2.5: Different scanning procedures for scanning a sample (violet box) from above (indicated by objective and probe beam): a) Depth profiles (A-scans) are recorded successively while the probe beam is moved along the first transversal axis (labelled "fast scanning direction"). Scanning along the slow scanning direction is necessary for a complete volume scan. b) The probe beam scans at a fixed depth along the first transversal axis to record a T-scan. The probe beam can then either be shifted along the other transversal axis to record a C-scan or along the depth to record a B-scan.

Moving particles influence the phase of the reflected light. For example, the phase difference detected between two measurements (such as two A-scans) can be calculated via

$$\Delta\phi = 2\, n\, v\, k\, \tau \cos(\beta) \tag{2.10}$$

with $k = 2\pi/\lambda$, λ being the central wavelength of the used light source, n the refractive index of the sample, τ the time between two A-lines and β the angle between the probing light beam and the moving particle trajectory.

The minimum detectable velocity depends on the signal-to-noise ratio ([24], [25]). This is because flow velocities corresponding to phase changes below the standard deviation of the phase cannot be distinguished from measurement noise. Equation 2.11 gives the relation between Signal-to-Noise ratio SNR and the standard deviation of the phase $\sigma_{\Delta\phi}$:

$$\sigma^2_{\Delta\phi} = \frac{1}{SNR} \tag{2.11}$$

Combined with equation 2.10, this gives v_{min} as:

$$v_{min} = \frac{1}{2\sqrt{SNR} \cdot n \cdot k \cdot \tau \cdot \cos(\beta)} \tag{2.12}$$

Further, a maximum velocity that is not phase-wrapped can be calculated from the

wavelength, the refractive index and the time between two measurements ([26]):

$$v_{max} = \frac{\lambda}{2n\Delta t \cos(\beta)} \tag{2.13}$$

Velocities larger than v_{max} cause phase shifts larger than 2π, which are therefore ambiguous. In an OCT experiment, the time Δt can be chosen and varied by the experimenter quite easily and within a relatively large range by altering the imaging or detection protocol. The light source (providing λ) and sample type (defining n) are usually fixed.

The general idea of the "multiple measurements method" is to compare images acquired from the same location. Static tissue appears the same in all images (neglecting motion of the sample) while the signal from moving tissue varies. With the considerations about detectable flow velocities given above, and bearing in mind that *in-vivo* measurements are susceptible to movements of the whole sample, the typical way to detect vessels in OCT is to perform OCT angiography. Thereby B-scans that are recorded at the same location but separated in time are compared. Modern systems are too fast to detect capillary flows between consecutive A-scans (measurement times of 10 µs) but too slow to compare complete volume scans (recording time of several seconds, during which a live sample moves too strongly).

Chapter 3

Materials and Methods

3.1 The experimental setup

Experiments were performed on a Fourier-Domain OCT system consisting of a fiber-based Michelson-interferometer and a bulk-optics spectrometer (see fig. 3.1). The light source was a AFC Technologies BBS 1310 B-TS broadband light source with a center wavelength of 1310 nm and a spectral width of 50 nm. The Michelson-type interferometer consists of a 50:50 fiber based beam splitter. The fibers are single-mode fibers and 3-paddle polarization controllers are used in the reference and the sample arm in order to match the polarization state of the light returning from both arms. The reference arm (see figure3.2) consists of a fiber collimator and a flat mirror which is mounted on a translation stage. The mean length of the reference arm is about 15 cm and can be varied by about 3 cm. In the sample arm (see figure3.3), two galvanometer scanners were placed to enable volumetric scanning of the sample. After the scanners, a focusing lens was placed (focal lengths of 5 and 2 cm were tested). The spectrometer (see figure3.4) consists of a first lens for collimation of the beam exiting the fiber (focal length 50 mm), a transmission grating, a second lens (focal length 180 mm) and a line-scan camera. Both lenses are achromatic in order to minimize chromatic aberrations. As transmission grating, a HD 1145l/mm grating with 25.4 mm diameter from Wasatch Photonics was installed. The camera is the model SU1024-LDH2 from Goodrich (now UTC aerospace systems), a high-speed 1024-pixel linescan InGaAs camera with an A-line rate of about 91 kHz.

3.2 Imaging protocol

The imaging protocol used for all presented experiments acquired 4 repeated B-Scans at each of 500 different locations (orthogonal to the B-scan direction), with each B-Scan containing 500 A-Scans. This totals one million of 1024-pixels-wide A-Scans per recording. Acquisition time for a single A-scan is about 11 µs, so the complete recording of the volume takes about 11 s. During this time, the sample has to remain as steady as possible (see figure 3.5 for an image of the handrest used for this purpose). Image acquisition was triggered by the 91 kHz line-scan camera. The galvanometer scanners were driven with a FPGA board. The corresponding FPGA program was

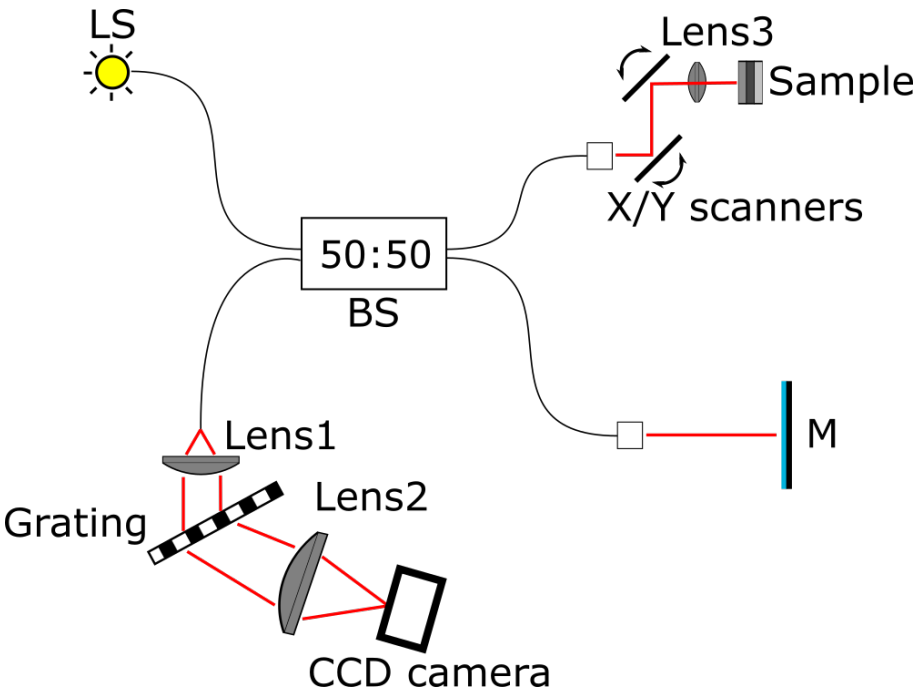

Figure 3.1: The FD-OCT-setup is a fiber-based Michelson interferometer with a 50:50 fiber beam splitter (BS). The light source is directly coupled to the fiber, the reference and sample arms end in fiber collimators. The reference arm consists of a mirror M on a translatable stage for adjustment of the coherence gate (axial depth position of the A-scan). The sample arm consists of two galvanometer scanner mirrors, a focussing lens and a mount for the sample. The spectrometer arm consists of two lenses, a transmission grating and a CCD linescan camera.

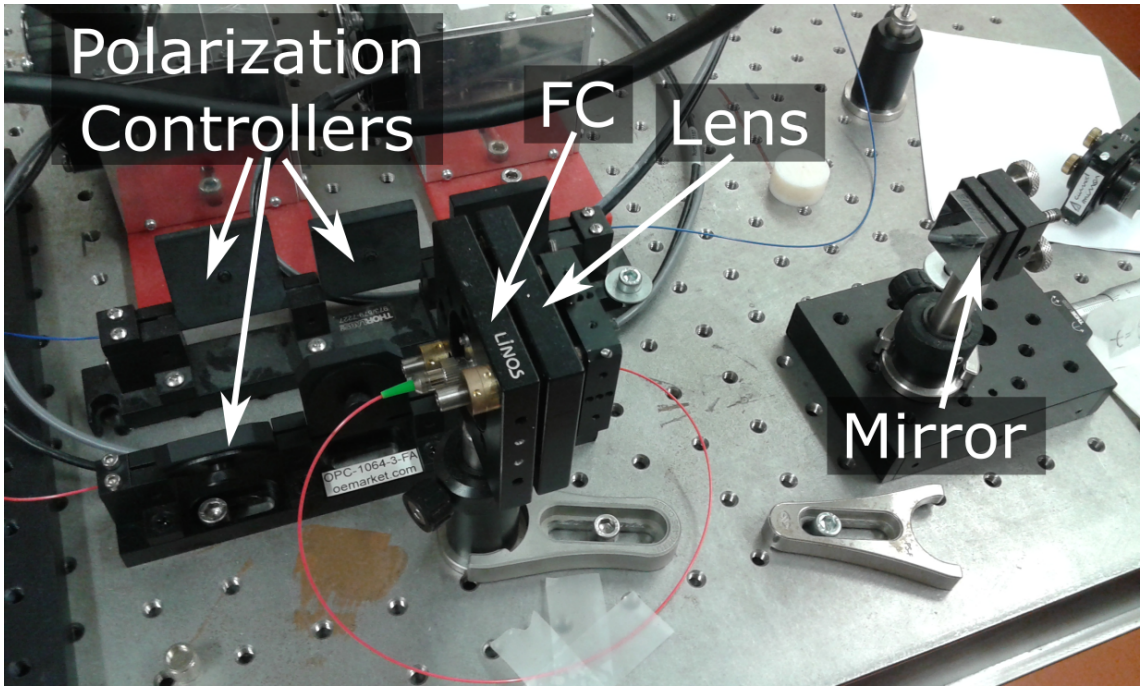

Figure 3.2: Photograph of the reference arm of the setup.

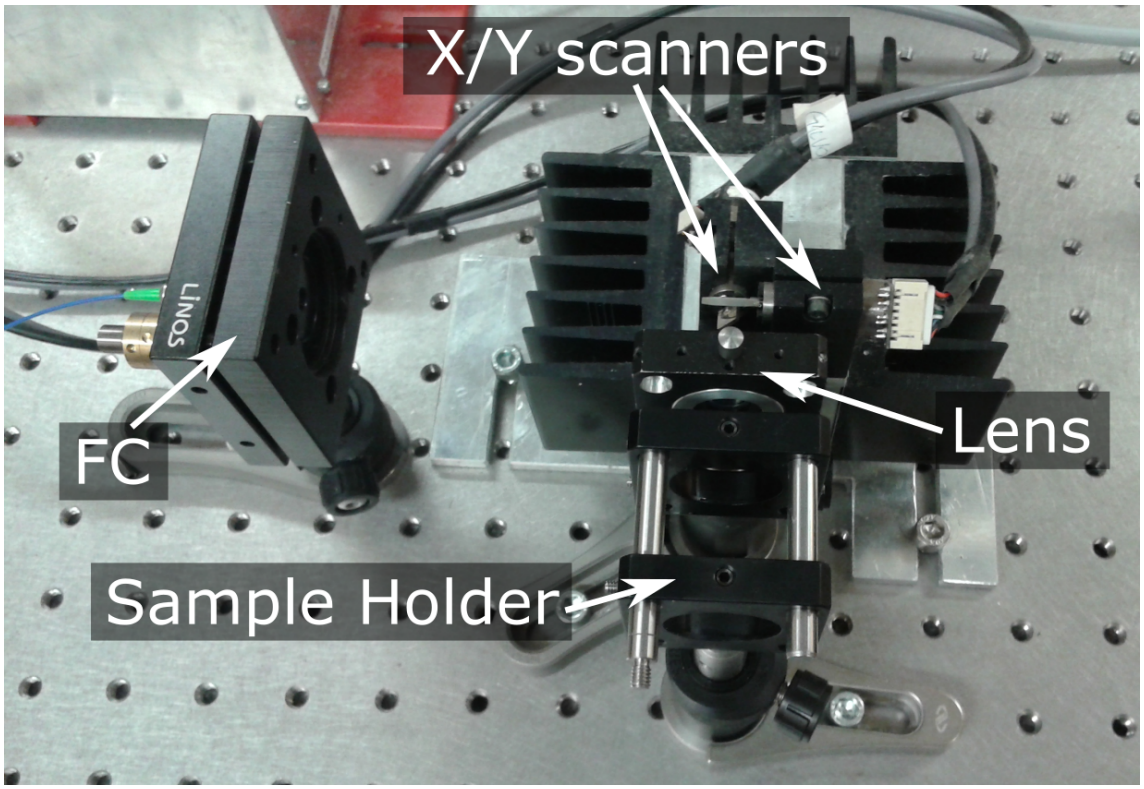

Figure 3.3: Photograph of the sample arm of the setup: the fiber collimator (FC), the galvanometer scanner mirrors (X/Y scanners) and the focussing lens.

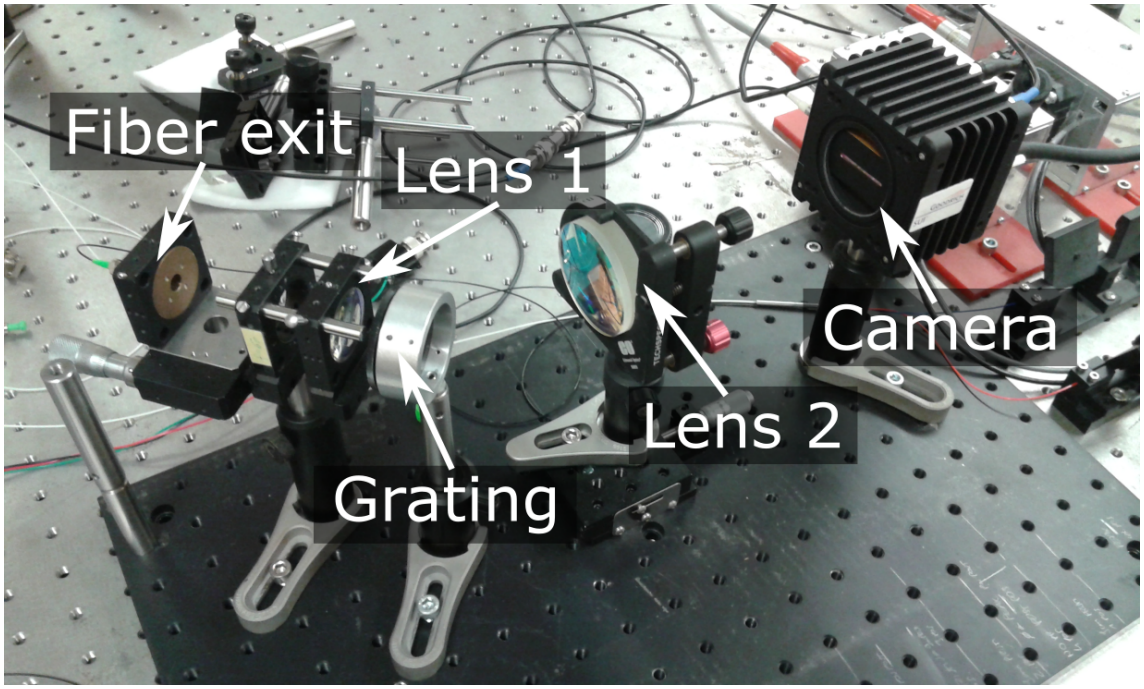

Figure 3.4: Photograph of the spectrometer arm of the setup

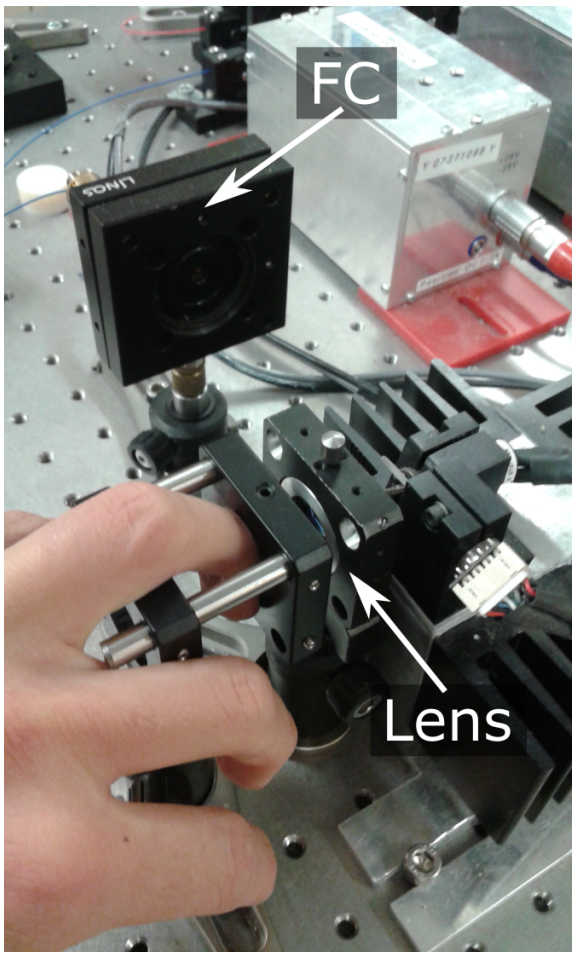

Figure 3.5: The sample arm during an in-vivo measurement of the nailfold region (FC, the fiber collimator of the sample arm, and the lens are labelled).

already available for this thesis. For in-vivo skin images, three skin conditions were tested:

- Bare skin
- Ultra-sound contact gel applied to the skin
- Olive oil applied to the skin

Imaging a completely unaltered skin surface would best meet the requirements of an non-invasive method. However, matching the refractive indices of skin and air by introducing a layer of gel or oil in between reduces surface reflections (see 2.2). Ultra-sound gel is a safe and tested medicine product and vegetable oils are commonly used in capillaroscopy ([18]).

The ultra-sound gel used was the *Sonomed* gel by Meditrade Medicare Medizinprodukte GmbH & Co KG, consisting of aqua, propylene glycol, carbomer, benzylalcohol, methylchloroisothiazolinone, methylisothiazolinone.

A-scan data was recorded via an available LabView program on a standard PC.

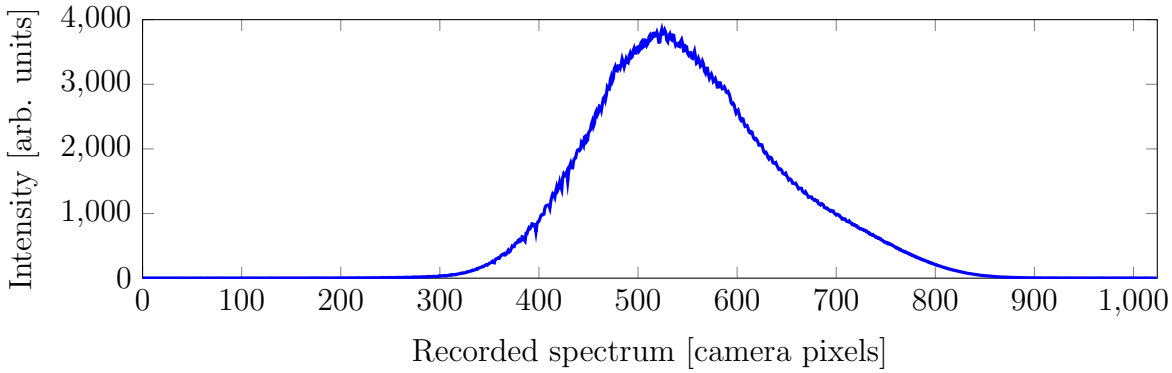

Figure 3.6: Average of 500 A-scans belonging to one B-scan.

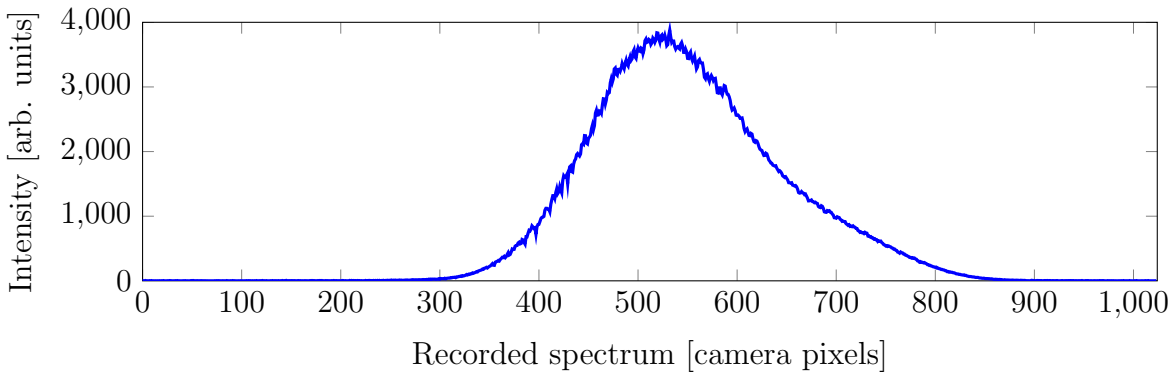

Figure 3.7: Recorded spectrum of a single A-scan. The modulation pattern imprinted by the interferometer is barely discernible against the emission spectrum background.

3.3 Post-Processing

3.3.1 Image creation

The raw data was saved in a tiff file containing 1000000x1024 pixels.

A LabView program was developed to separate single, raw data containing the information of single B-scans from that file (each B-scan consists of 500x1024 pixels). The spectral data was then averaged along the B-scan direction to generate the spectrum of the light source inlcuding autocorrelation terms (such as static reflexes) from the reference arm (see figure 3.6). This averaged spectrum was then subtracted from the spectral data of each single A-Scan to remove the autocorrelation terms and the DC-term of the spectrum. The resulting spectrum in λ-space was then converted to k-space via a rescaling algorithm (see figures 3.8 and 3.9, respectively). Finally, Fast-Fourier-Transforms were used to convert the spectral information into spatial information (an A-scan). As the Fourier-Transform is symmetric (positive or negative path length differences between sample and reference arm cannot be distinguished), half of the entire length (half of the 1024-pixel recording) can be dropped, yielding the final 512-pixel-A-scans (as shown in figure 3.10). Conversion of the data to gray-scale-values and combining 500 adjacent A-Scans gives a 500x512 pixel B-scan, as shown in figure 3.11. Because of the high dynamic range, values

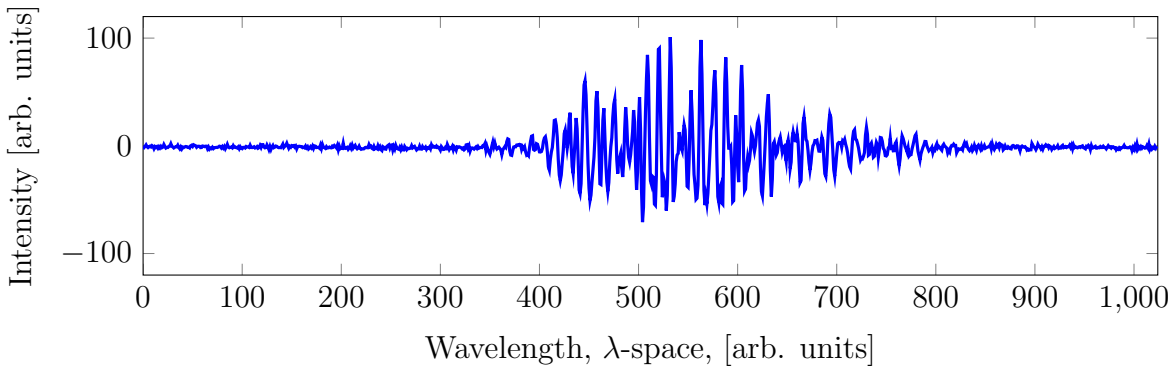

Figure 3.8: Recorded spectrum 3.7 after subtraction of the average spectrum (average over 500 adjacent A-scans, such as in figure 3.6). The modulation pattern is now visible.

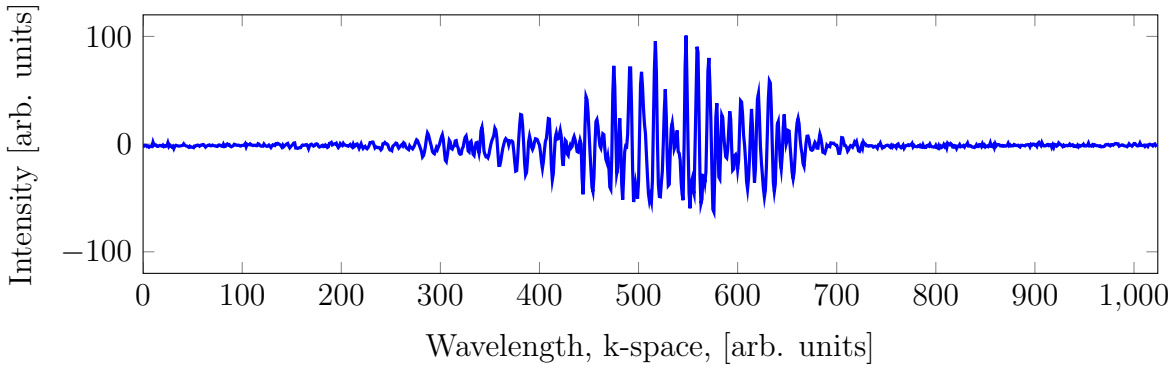

Figure 3.9: The pattern from figure 3.8 was rescaled to wavenumber k instead of wavelength λ.

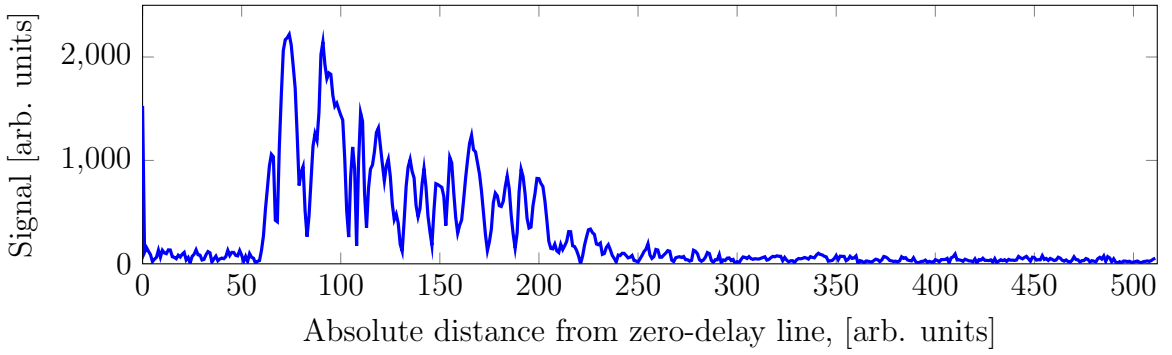

Figure 3.10: The final A-scan data from which images can be formed. The Fourier-Transformation of figure 3.9 yields spatial information about the position of reflective layers in the sample (peaks in this figure).

need to be converted to a logarithmic scale. These images contain the structural information on the sample.

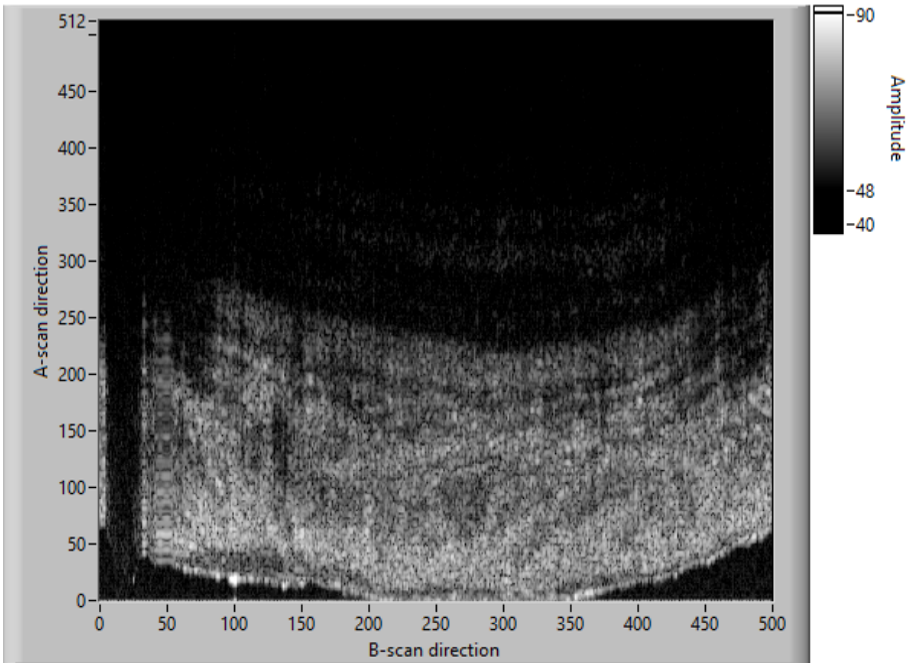

Figure 3.11: One B-scan as displayed in the Labview-program used for data post-processing.

3.3.2 Sample motion compensation

For detection of motion as outlined above it is essential that several B-scans are recorded at exactly the same location. To account for small sample movements, the following correction algorithm was employed:

- Computation of the cross-correlation between subsequent B-scan images.
- Detection of the peak of the cross-correlation function.
- Calculate a vector $\vec{s}$ as the vector pointing from the peak of the cross-correlation-function to the center of the cross-correlation-map.
- Shifting of the second image along $\vec{s}$.

3.3.3 En-Face images and Surface detection

En-Face images can be created by projecting each A-Scan onto a single point (for example through averaging along an A-scan). This turns a volumetric data set into a 2-dimensional image. A simple algorithm is to add up all values along the A-scan. To create an image of the sample surface, it is beneficial to only add up data originating from close vicinity of the sample's surface. On the other hand, if

an image of structures below the surface is desired, it is beneficial *not* to add these data points. This is even more important as signal from the surface tends to be larger (sometimes the signal from the surface might be saturated) than from within the sample. For this purpose, a surface-detection algorithm was implemented in LabView:

- Find the first pixel of the A-scan profile that has a higher value than a certain threshold *and* constitutes a local maximum.
- Connect these points along the B-scan.
- Apply a sliding-window minimum filter (optional, this is to ensure that the surface is detected rather outside the sample than within).
- Average this boundary function over the 4 images from the same location.
- Smooth out this averaged boundary function (eliminate outliers) by use of a median filter.

The surface coordinates were then used to define a range relative to the surface. Only data from within that range was included in further analysis.

3.3.4 Vessel detection

To perform angiography, the simplest method is to compute the difference between two B-scans from the same location. Figures 3.13a and 3.13b display two such B-scans and figure 3.13c the resulting difference image. As 4 images were recorded per location, 3 differences could be computed (figure 3.12 shows a flow-chart of the whole algorithm). These were then averaged in order to increase the signal to noise ratio of the angiographic data. The improvement is illustrated by comparison of figure 3.13c to 3.13d In the resulting image, all values below a certain threshold were set to zero. This further reduces noise in the angiographic image.

More sophisticated methods to perform angiography also employ the phase information from the complex image. An exemplary image is shown in figure 3.14. The image was generated in LabView by extracting the phase information from the result of the Fourier-Transform and calculating the phase difference between two consecutive B-scans. As 4 images from the same location were recorded, 3 such differences could be calculated and were averaged. Furthermore, the mean phase (averaged over all A-scans in the image) was subtracted from the image. Static tissue causes a constant phase shift while the flow within vessels adds a random fluctuation. Vessels should then be discernible in the image by e.g. searching for pixel areas with high standard deviation (but high signal amplitude, as noise also adds random phase fluctuations). However, for the collected data, none of these methods provided a significant improvement in vessel contrast to justify the increased computation time. Therefore these results were omitted in the following.

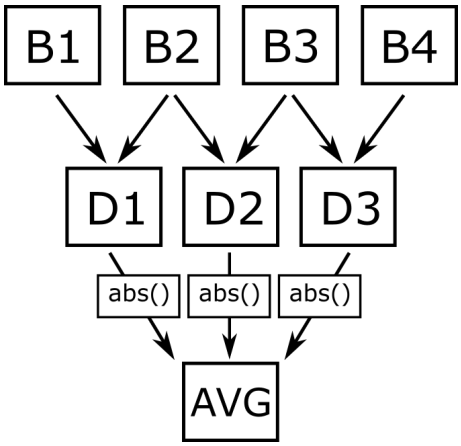

Figure 3.12: A flowchart of the algorithm used to perform angiography from 4 B-scans recorded at the same location. The B-scans B1-4 are subtracted from each other to create D1-3. The absolute values of these are then averaged to obtain the final angiographic image.

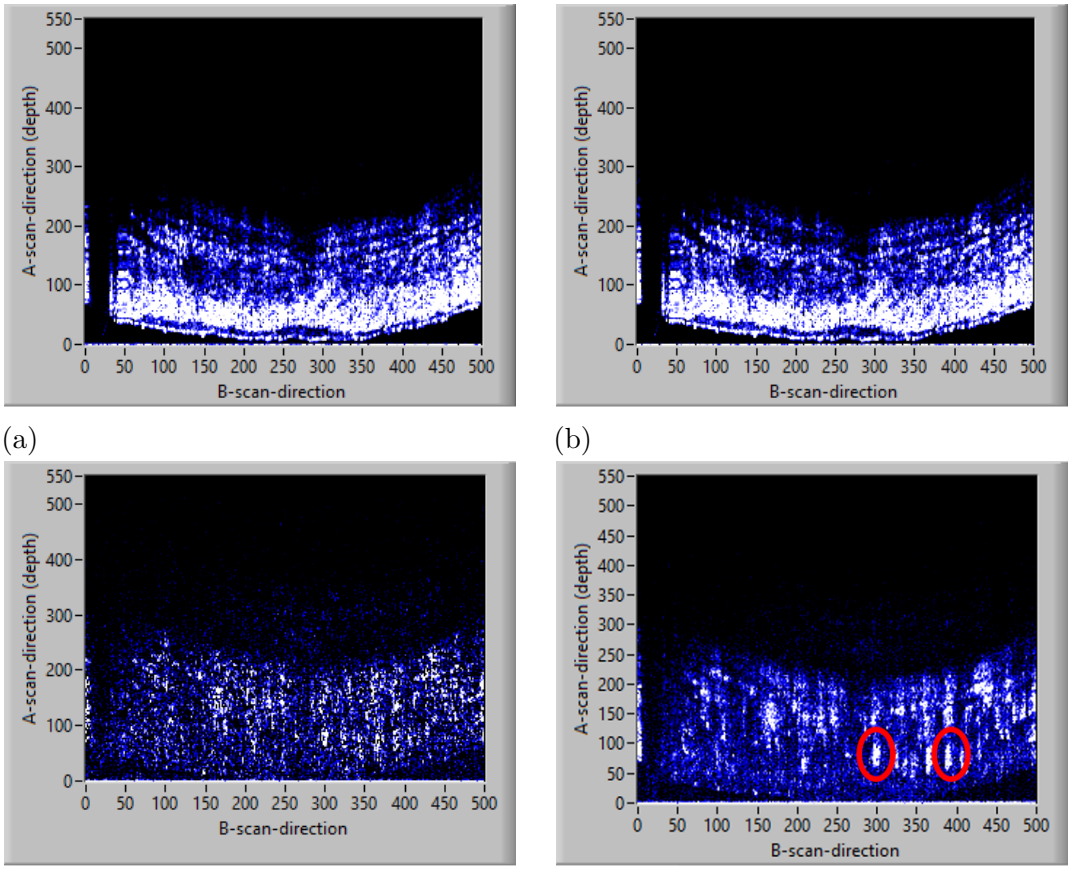

Figure 3.13: Vessel detection from B-scan data: a) and b) show two B-scans from which c) was computed by subtracting b) from a). d) is the average of 3 such difference-images, where individual vessels can already be detected (white spots, two examples circled)

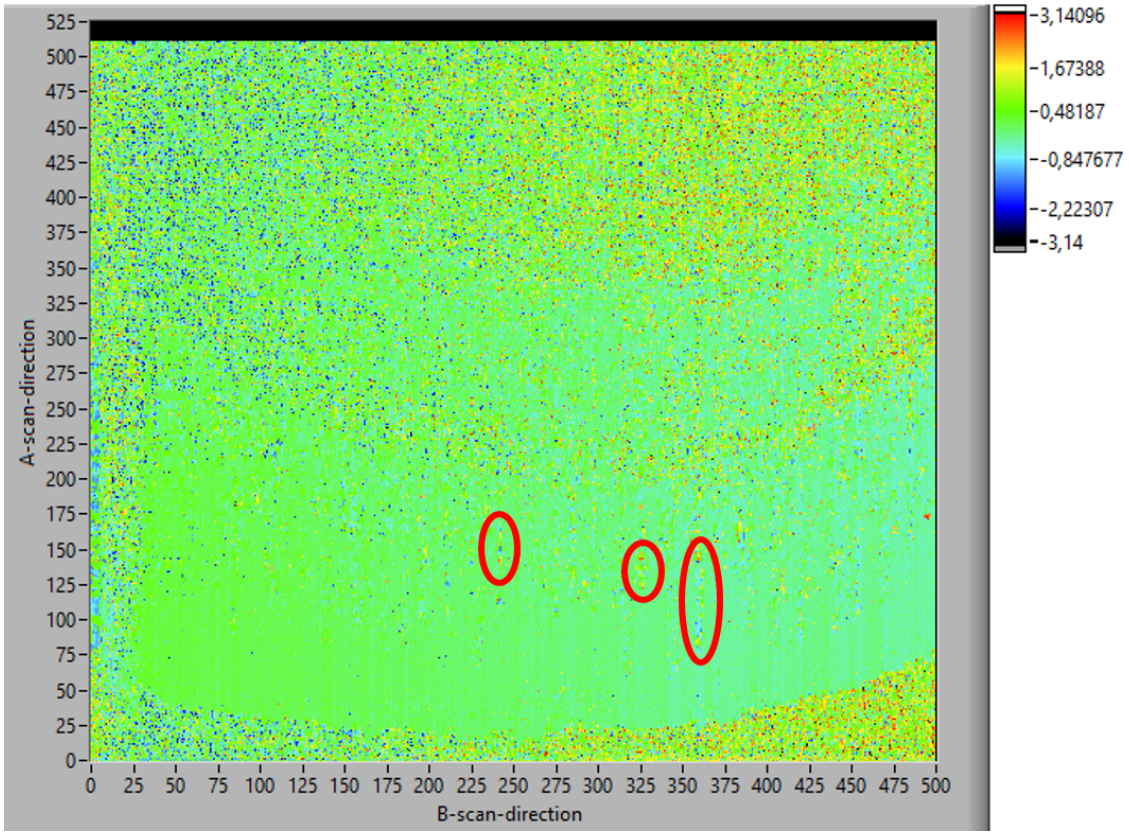

Figure 3.14: Phase difference image between two successive B-scans. In this false-colored image, phase variations caused by blood flow within the capillaries are visible (three examples are marked by red circles). However, the results were not consistent and reproducible enough to perform angiography.

3.4 Overview of the experiments

Determination of the signal-to-noise-ratio and sensitivity roll-off

The signal-to-noise-ratio of an OCT system is a critical parameter for all other experiments. The theoretically achievable sensitivity was calculated as described above and used as reference for the measured sensitivity.

Resolution and field of view

Determination of the lateral resolution was done experimentally by imaging a resolution test target. From that, the field of view was calculated.

Polarization state

The influence of the polarization state of the light in the reference and sample arm, respectively, on the image quality was tested. The polarization state can be adjusted using the polarization controller paddles. The hypothesis was, that there should only be negligable influence, as the light source is supposed to provide mostly unpolarized light.

In-vivo tomography imaging of human skin

In-vivo structural OCT images from various skin areas have been recorded. In theory, the thickness of the various skin layers should differ from region to region and this difference should be visible in the tomographic images.

In-vivo angiography of human nailfold

In these experiments, the capillaries in the human nailfold have been imaged. Pathologies in the capillaries of the nailfold can be of diagnostic value in clinical practice. A wide field of view while still maintaining the capability of resolving individual capillaries and possibly even capillary loops (see 2.1) is desirable.

Further, the reproducibility of the method has been investigated to verify that true structures are imaged. To do this, repeated measurements have been taken and the results have been compared. In the optimal case, the different measurements yield similar results.

Chapter 4

Results

4.1 Spectrometer efficiency

To estimate the spectrometer efficiency, the optical power at the entrance of the spectrometer (emitted from the end of the optical fiber at the interferometer exit) was measured and compared with the power detected by the camera. For this measurement, the light in the sample arm of the interferometer was blocked and the reference arm mirror was adjusted to maximize the signal on the camera but not to saturate it. The output power at the interferometer exit was measured with a Thorlabs PM 100 D powermeter and was $P_{spectrometer} = 77\,\mu\text{W}$. To calculate the power incident on the camera, a spectrum was recorded using the setup and LabView as described in chapter 3. The area $A_{spectrum}$ under the curve was then calculated in LabView by integration of the pixel values and dividing by the bit depth. Multiplying this area with the full-well-capacity of the camera (of 1870 electrons/count) gives:

$$N_{electrons} = A_{spectrum} \cdot 1870\,\text{electrons/count} \tag{4.1}$$

This corresponds to an energy of

$$E_{spectrum} = \frac{N_{electrons}}{\eta} \cdot E_\nu \tag{4.2}$$

with $\eta = 0.85$ being the quantum efficiency of the camera and E_ν the energy of a single photon. $E_\nu = h \cdot \nu = \frac{h \cdot c}{\lambda}$ can be calculated from the central wavelength $\lambda = 1300\,\text{nm}$ of the incident light, the speed of light in vacuum $c = 299792458\,\text{m/s}$ and the Planck constant $h = 6.626 \cdot 10^{-34}\,\text{m}^2\text{kg/s}$. Dividing the energy of the recorded spectrum by the exposure time $\tau = 6.96\,\mu\text{s}$ yields

$$P_{camera} = \frac{E_{spectrum}}{\tau} = 41.2\,\mu\text{W} \tag{4.3}$$

The spectrometer efficiency ρ is therefore

$$\rho = \frac{P_{camera}}{P_{spectrometer}} = \frac{41.2}{77} = 0.54 \tag{4.4}$$

4.2 Signal to noise ratio and sensitivity roll-off

The theoretical, shot-noise-limited signal-to-noise-ratio (SNR) of an FD-OCT system can be calculated using the following formula (compare [14] and [23])

$$SNR = \frac{\eta \cdot \rho \cdot P_{sample} \cdot \tau}{E_\nu} \tag{4.5}$$

$P_{sample} = 0.4\,\mu\text{W}$ is the power arriving at the spectrometer reflected from mirror in the sample arm and was measured with a powermeter while the reference arm was blocked. For η, ρ and E_ν, the values as given above were used. This yields a theoretical SNR of 69.14 dB for the presented system. These measurements required the use of an optical density filter in the sample beam path to avoid saturation of the camera. Since that filter is not present in following experiments, its relative attenuation was also measured and added to the SNR value. Power was measured before (10.6 mW) and after (22 µW) the neutral density filter. Because light has to pass the filter twice, an attenuation value of

$$Att = 2 \cdot 10 \cdot \log_{10}(\frac{10.6}{0.022}) = 53\,\text{dB} \tag{4.6}$$

has to be added to the measured SNR. Overall, this gives a maximum achievable shot-noise-limited signal-to-noise ratio of 122.1 dB.

To measure the *actual* SNR of the system, the maximum signal peak of the already Fourier-transformed OCT-signal was compared to the standard deviation of the noise in the signal. For this measurement, a mirror was placed in the sample arm and the signal was processed and evaluated in LabView. SNR can be calculated as

$$SNR = 2 \cdot 10 \cdot \log_{10}(8000/6) + Att = 63\,\text{dB} + 53\,\text{dB} = 116\,\text{dB} \tag{4.7}$$

This is quite close to the shot-noise-limit. The factor 2 accounts for the fact that the relevant physical quantity is the *intensity* of the incident light. As the amplitude is being measured and intensity is proportional to the square of the amplitude, the logarithmic value can just be doubled.

To measure the sensitivity roll-off of the system, a mirror was placed in the sample arm of the interferometer in a position that maximizes the recorded signal. By moving the reference arm mirror away from the zero-delay position, the signal amplitude decreases. This is due to optical resolution limits and finite pixel width of the camera ([27]). The SNR was measured at 12 displacement positions of the reference mirror in the range of $0 - 2$ mm. Figure 4.1 shows the roll-off of the sensitivy of the system. Noise does not change considerably with imaging depth. The average roll-off was calculated as 9.92 dB/mm.

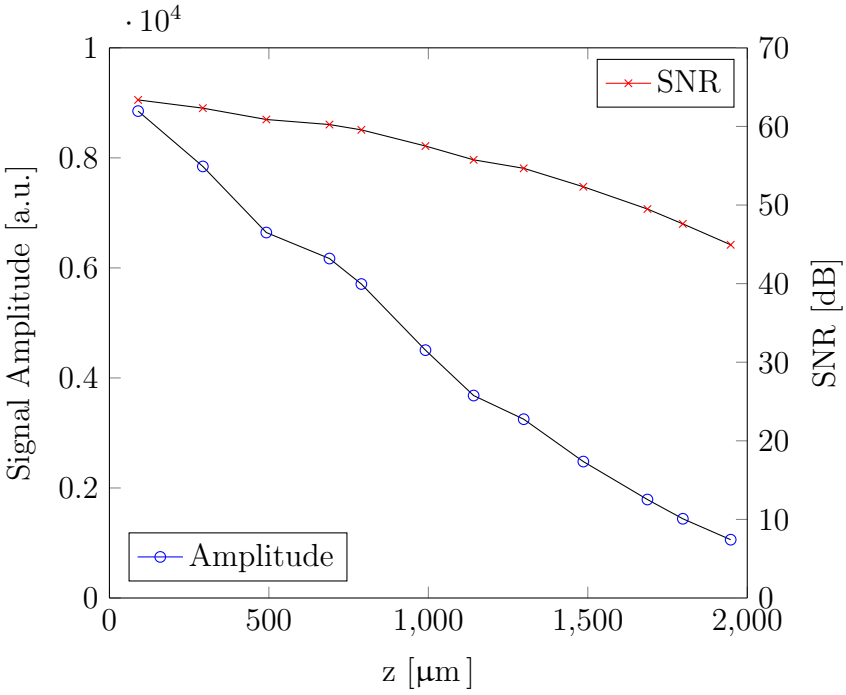

Figure 4.1: The sensitivy roll-off of the SD-OCT system.

4.3 Resolution and field of view

The actual resolution of the system was measured by imaging the USAF 1951 Resolution test target (Thorlabs). Measurements were taken for the different used scanning protocols. Data was recorded using the exact same protocols as in the subsequent experiments. The recorded spectra were processed in LabView according to the procedure given above and exported as images. The images were rescliced (transformation of a stack of B-scans into a stack of C-scans) and averaged along the A-scan direction in ImageJ in order to generate en-face projection images. Figure 4.2 shows the resulting images for the 2 cm lens in the sample arm and the 6000x6000 (arbitrary numbers for the FPGA program) scanning protocol.

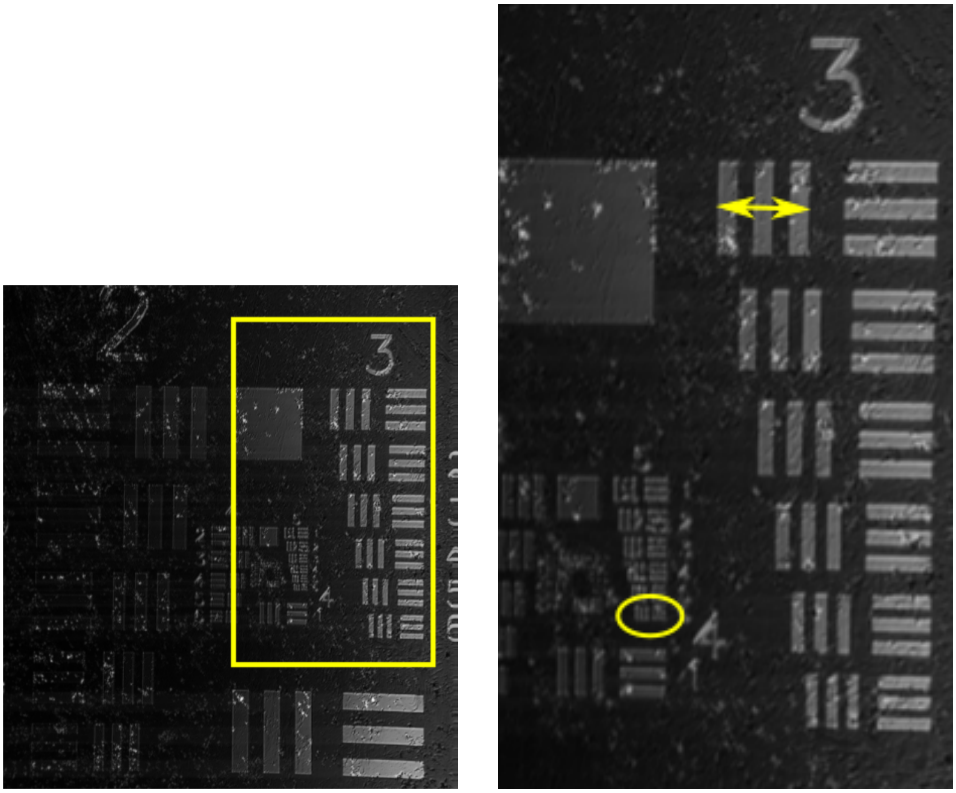

(a) (b)

Figure 4.2: Image of the resolution test target. The elements that were used for quantification of resolution and field of view are element 6 of group 5 and element 1 of group 3, respectively. a) The complete image of the resolution test target, the indicated rectangle is shown enlarged in b). b) Enlarged and cropped part of the image, the elements used to determine the resolution are circled. The double arrow indicates the element used for scaling the image (and thereby the Field of View).

Element 6 of group 5 was the largest non-resolvable element. Since that element consists of lines with a density of 57 line-pairs/mm, the resolution-limit of our system is about 17.5 µm.

The field of view can be calculated from a set of larger lines. The lines of element 1 from group 3 are known to measure 62.5 µm (8 line-pairs/mm). To reduce random

error, the measurement was taken over the whole element (5 line widths: 3 lines and 2 equally wide spaces), which is 312.5 µm wide. Since the elements had a width of 40 pixels in the image, the image scale is 0.128 px/µm. The field of view is a square with a length of 500 pixels or 3.9 mm.

The 3000x3000 scanning protocol was evaluated accordingly (data not shown). Element 2 of group 6 was the largest non-resolvable element, yielding a resolution of about 13.7 µm. The field of view was calculated as described above. Using the lines of element 2 from group 2, the image scale is 0.25 px/µm. The field of view is a square with a length of 500 pixels or 1.98 mm, which is roughly half the field of view compared to the 6000x6000 pattern.

As the 6000x6000 pattern offers a significantly larger field of view and not a significantly reduced resolution, it was used in the further experiments.

4.4 In-vivo imaging of human skin

4.4.1 Structural OCT images

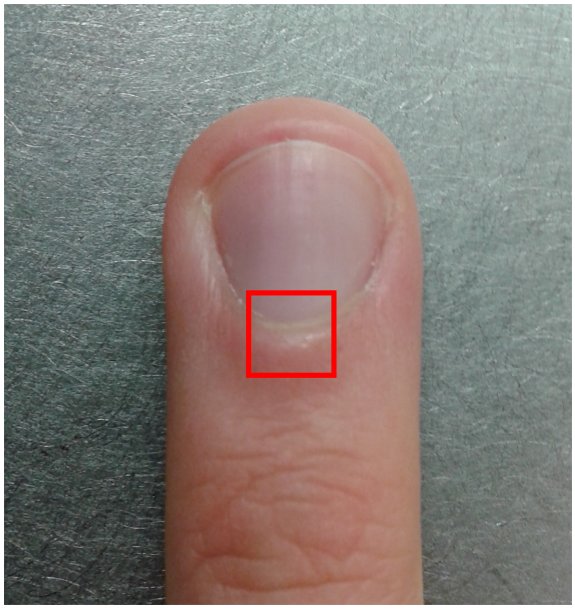

Figure 4.3: Photograph of a finger that has been imaged with the system, male subject, left ring finger. The nailfold region that was imaged is indicated by a red rectangle.

The presented system was used to acquire in-vivo images of the human skin at different locations: The nailfold (figure 4.4), the ventral side of the finger (figure 4.5), the lateral side of the finger(figure 4.6), the nail (figure 4.7). Various layers can be identified in the images: The stratum corneum, the granular cell layer, the spinous cell layer, the basal cell layer (which form the epidermis) and the beginning of the dermis. To visualize skin structures, multiple amplitude-B-scans were averaged in LabView. Then, the logarithm of the signal intensity was calculated to account for the high dynamic range of the original data. These experiments were also used to find a suitable skin treatment protocol, therefore some images were taken with olive oil and other with ultrasound gel applied on the skin. Also, the scanning protocol was adapted for most structural images: Scanning amplitude along the slow axis was set to $\frac{1}{20}$ of the amplitude along the fast axis. This gives more B-scans from the same area and allows for better averaging. Furthermore, figure 4.5 shows results from a scanning protocol with half the amplitude along the fast axis, resulting in a smaller field of view. In the last presented structural image (4.7), the angiography protocol was already used.

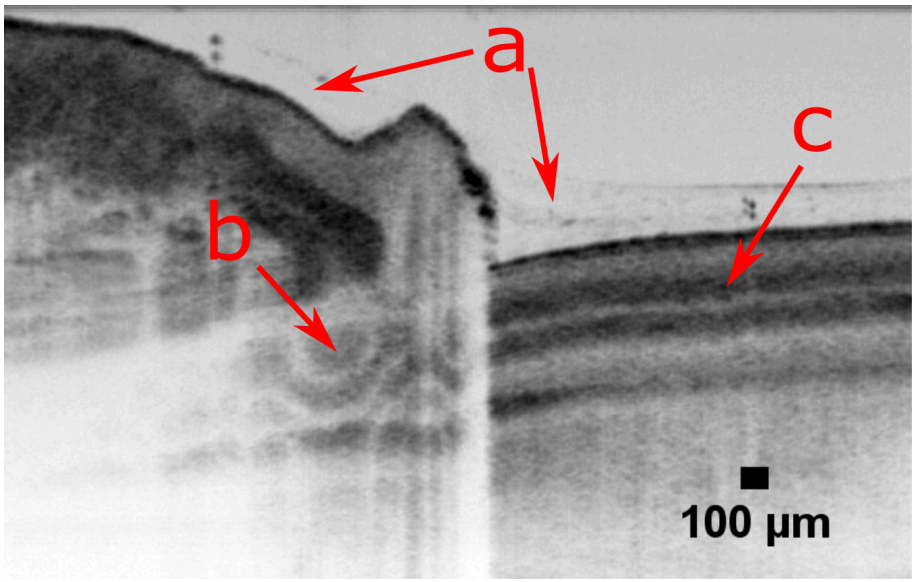

Figure 4.4: Structural image of the nailfold, treated with ultrasound gel applied to the surface, average of 250 B-scans. Arrows at a) mark the layer of ultrasound gel. The arrows at b) and c) mark ring and stripe artifacts that arise because of the birefringent properties of the nail.

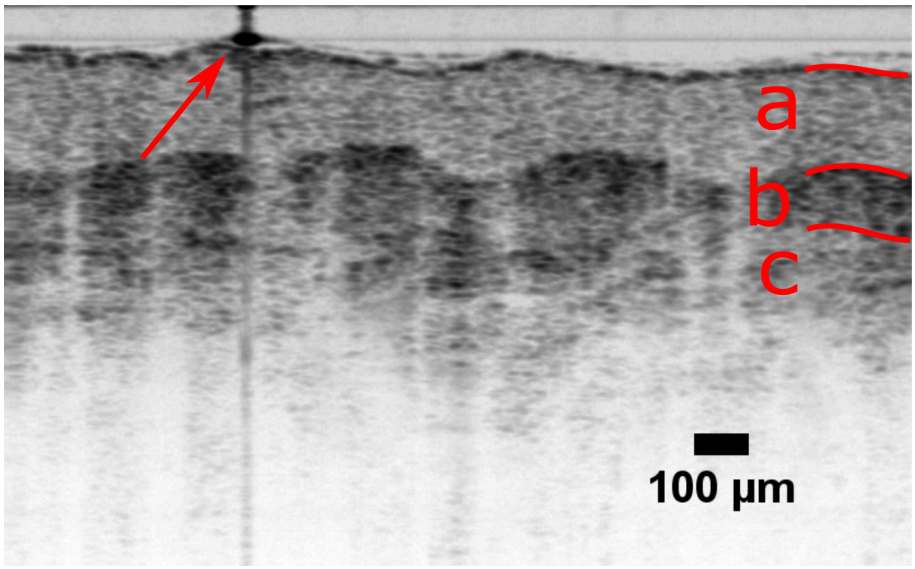

Figure 4.5: Ventral side of the finger, ultrasound gel has been applied to the surface in order to reduce the surface reflection, average of 80 B-scans. Note that this image has a different scale than the others as it was captured with a different scanning protocol. Skin layers are labeled a) Stratum corneum, the uppermost part of the epidermis, b) Stratum Granulosum, also part of the Epidermis and c) Beginning of the dermis. The arrow marks an artifact that arises from highly reflecting spots of ultrasound gel.

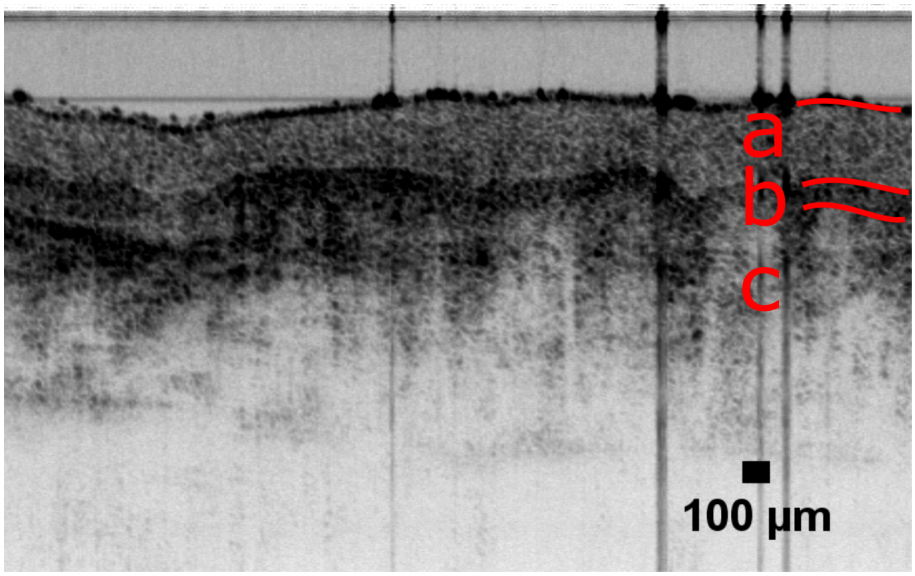

Figure 4.6: Lateral side of the finger, olive oil has been applied to the skin surface, average of 40 B-scans. Skin layers are labeled a) Stratum corneum, the uppermost part of the epidermis, b) Stratum Granulosum, also part of the Epidermis and c) Beginning of the dermis.

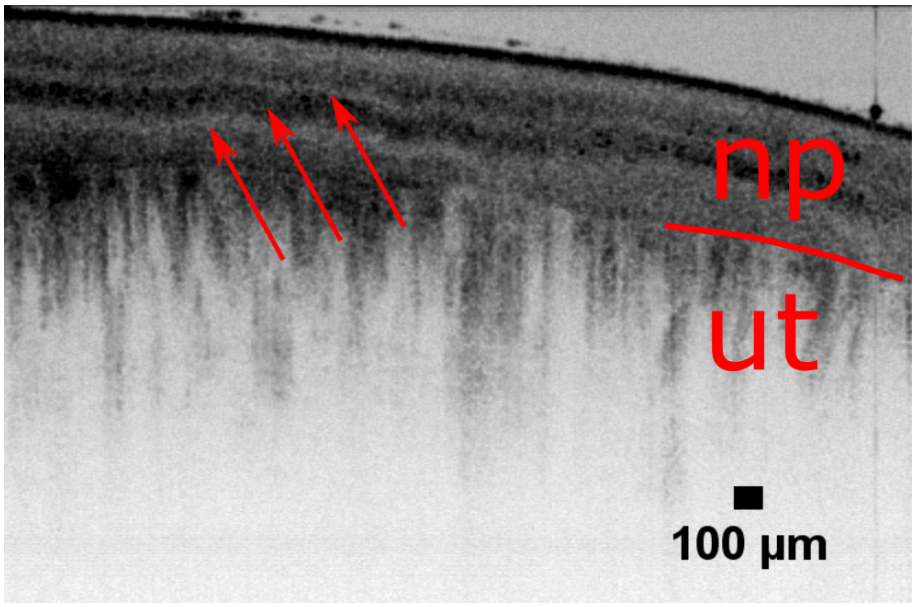

Figure 4.7: Structural image of the nail, olive oil has been applied to the skin surface, average of 40 B-scans, same scanning protocol as in the following angiography experiments. The nailplate (np) can be distinguished from the underlying tissue (ut). The horizontal stripes (indicated by arrows) in the nailplate originate from the birefringent properties of the nail substance.

4.4.2 Polarization measurements

A polarimeter was used to analyze the polarization properties of the light in the setup. Even though the light source is supposed to provide completely unpolarized light, a degree of polarization of up to 18% was measured. Using the polarization controller paddles in the reference and sample arm, it was possible to adjust the polarization to any desired state. In-vivo skin images were recorded for two special cases of illumination with linearly polarized light: The "cross-polarized" setting, where the direction of polarization in the sample arm is perpendicular to the direction of polarization in the reference arm, and the "co-polarized" setting, where the directions are parallel. Figure 4.8 shows the results of these settings. It can be seen, that surface reflections are reduced in the cross-polarized setting.

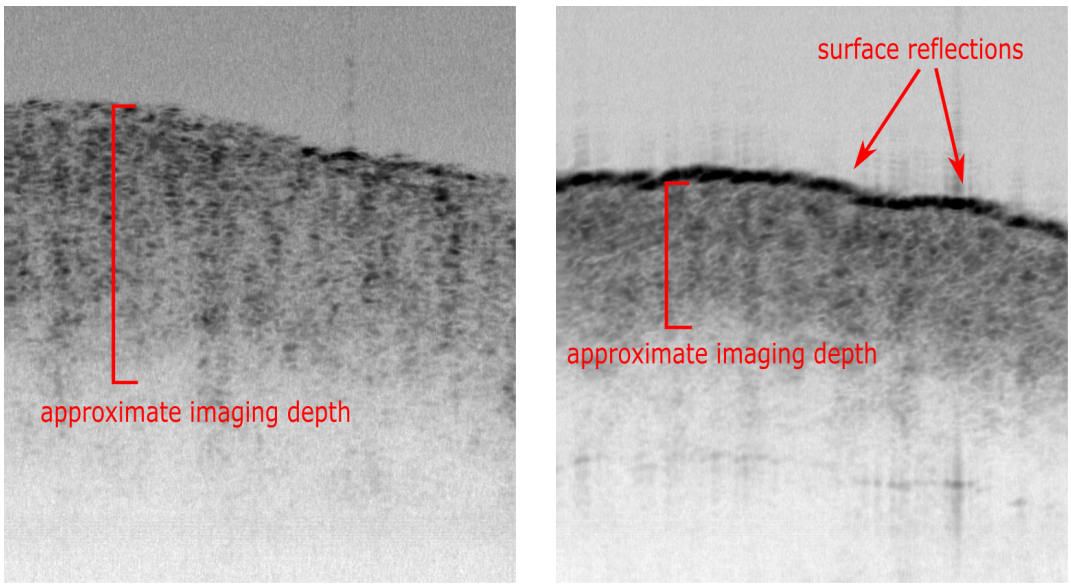

(a) (b)

Figure 4.8: Comparison of results obtained for two possible settings of the polarization controller paddles. a) results for a "cross-polarized" setting, b) results for a "co-polarized" setting. In the cross-polarized setting, surface signal and reflections are reduced and imaging depth appears greater. Both images are cropped averages over 10 B-scans from consecutive locations.

4.4.3 In-vivo angiography of human nailfold

To perform angiography, the B-scan method (see section 3.3.4) was tested on a subject. The subject was male, the ring finger of the left hand was treated with a drop of olive oil and imaged with the system. Figure 4.9 displays the results of the method for an average over 10 B-scans in adjacent locations: In figure 4.9a, the structural image is shown (obtained via averaging the 4 B-scans taken from the same location), while figure 4.9b shows the results of averaging the *differences* between the 4 B-scans taken from the same location. Figure 4.9c shows an overlay of these two images.

To create a vessel map from these B-scans, en-face projections were calculated. Figure 4.10 presents the final results of such an OCT angiographic recording. The data set was analysed as described (3.3) and single image slices were exported to be arranged in ImageJ. Figure 4.10a shows the structural en-face projection, figure 4.10b the en-face vessel map. Figure 4.10c is a composite of 4.10a and 4.10b using the "Red Hot" lookup-table offered by ImageJ. Individual capillary loops can be identified in the region closest to the nailfold.

Separation of vessel layers

A surface-detection algorithm was implemented in LabView (see section 3.3). This allows to separate information originating from different skin layers in post-processing. Without surface detection, automatic separation would be limited to horizontal planes, disregarding curvature of the finger. Figure 4.11 illustrates the functionality of the algorithm: Figures 4.11c and 4.11e show structural B-scans, the red line indicates the detected surface. The distance of the yellow lines to the surface can be chosen by the user. Vessel data is only calculated from the area between these borders. For figure 4.11d, the limit lines were set at 10 and 100 pixels distance to the surface (as shown in 4.11c). For figure 4.11f, the limit lines were set at 101 and 250 pixels distance to the surface (as shown in 4.11e).

Therefore, figures 4.11d and 4.11f display mutually exclusive information. It can be seen, that 4.11f displays a more connected network and larger vessels, while 4.11d displays more apexes. This is in line with anatomical considerations.

For clarity, figure 4.11a displays the location of the B-scans in the en-face image and figure 4.11b displays the complete vessel map.

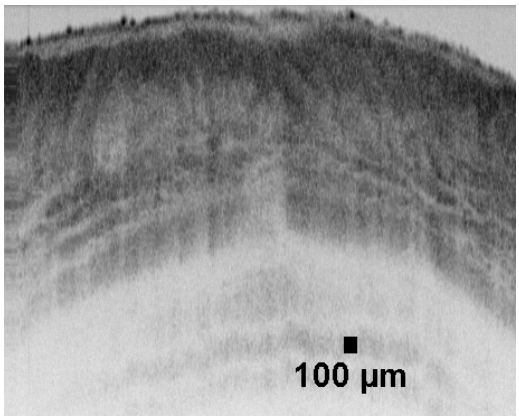

(a)

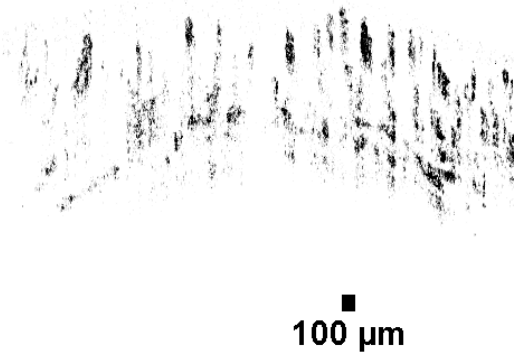

(b)

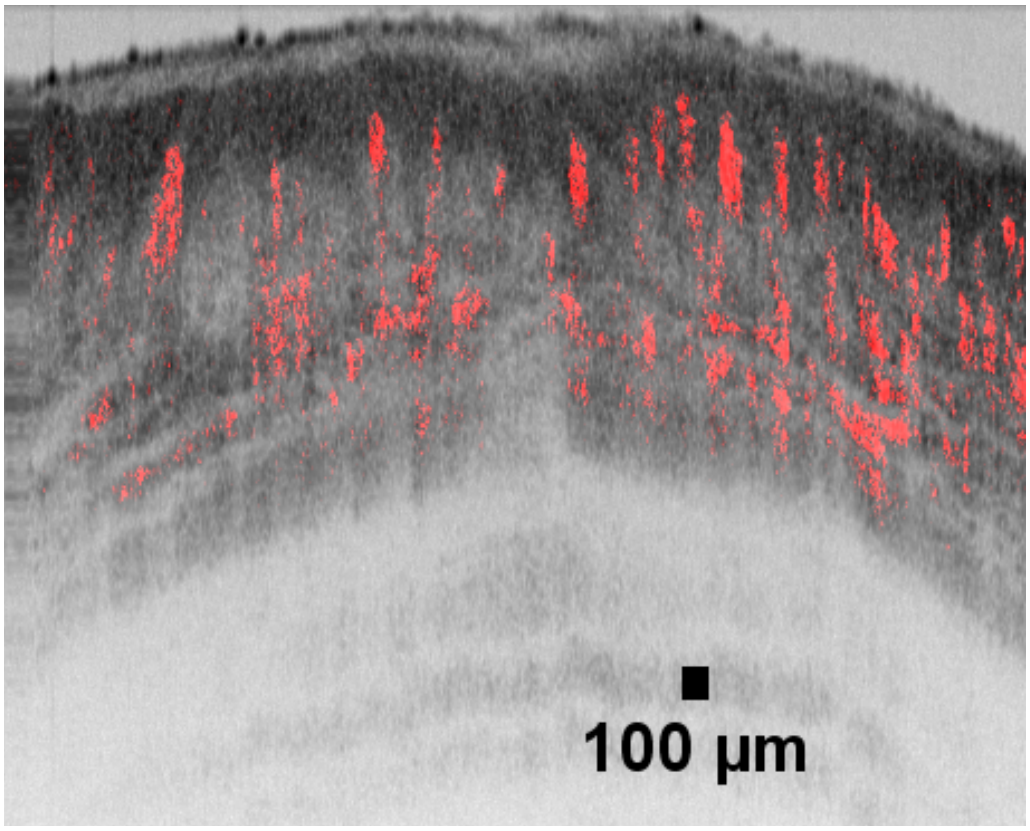

(c)

Figure 4.9: Average over 10 B-scan angiography images. a) shows the structural information (as presented in section 4.4.1, b) shows the angiography information computed via the B-scan method, as explained in section 3.3.4. c) composite image created in ImageJ (red indicates the vessels while the structural information is displayed on a logarithmic grey scale).

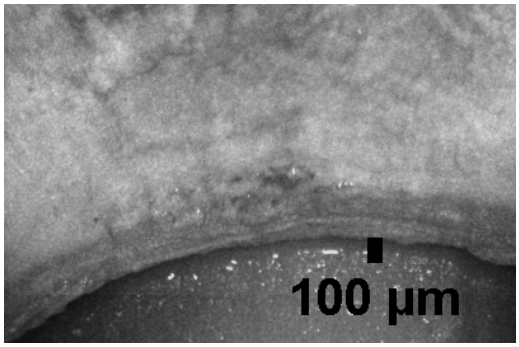

(a)

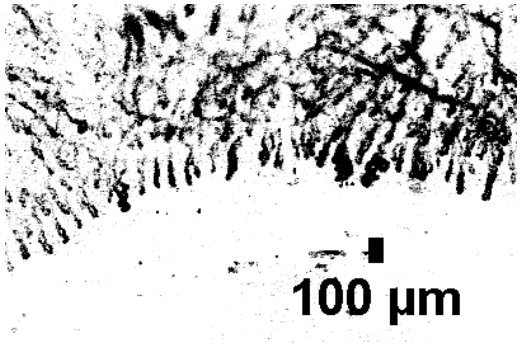

(b)

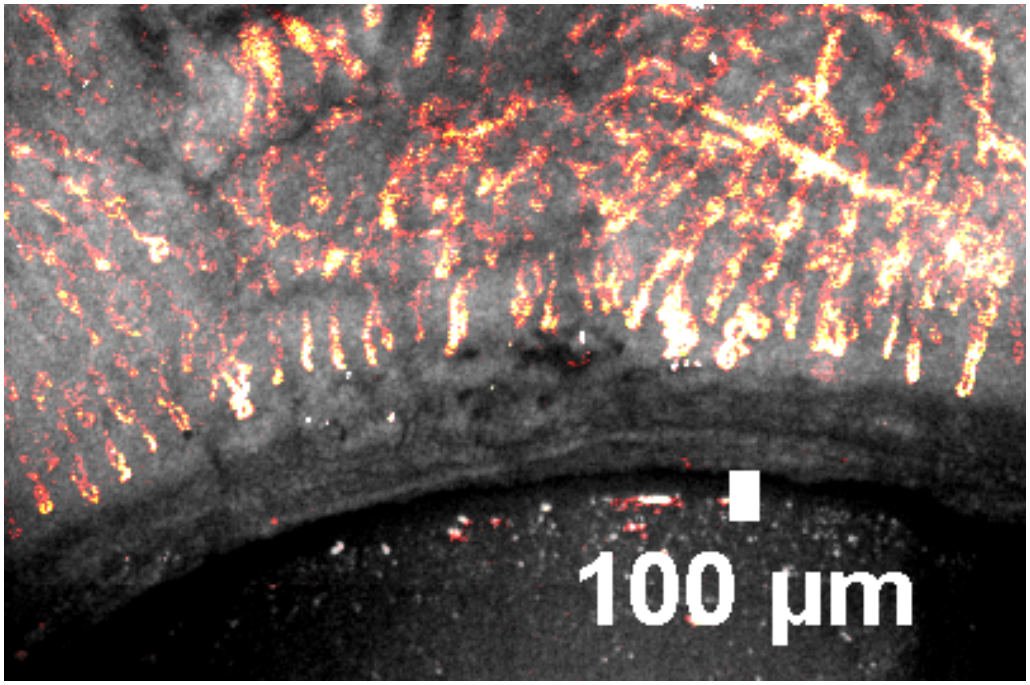

(c)

Figure 4.10: Angiography results from the presented system (cropped). a) Structural en-face image of the nailfold region, b) Vessel map of the same region, c) composite image showing the capillaries and the structure.

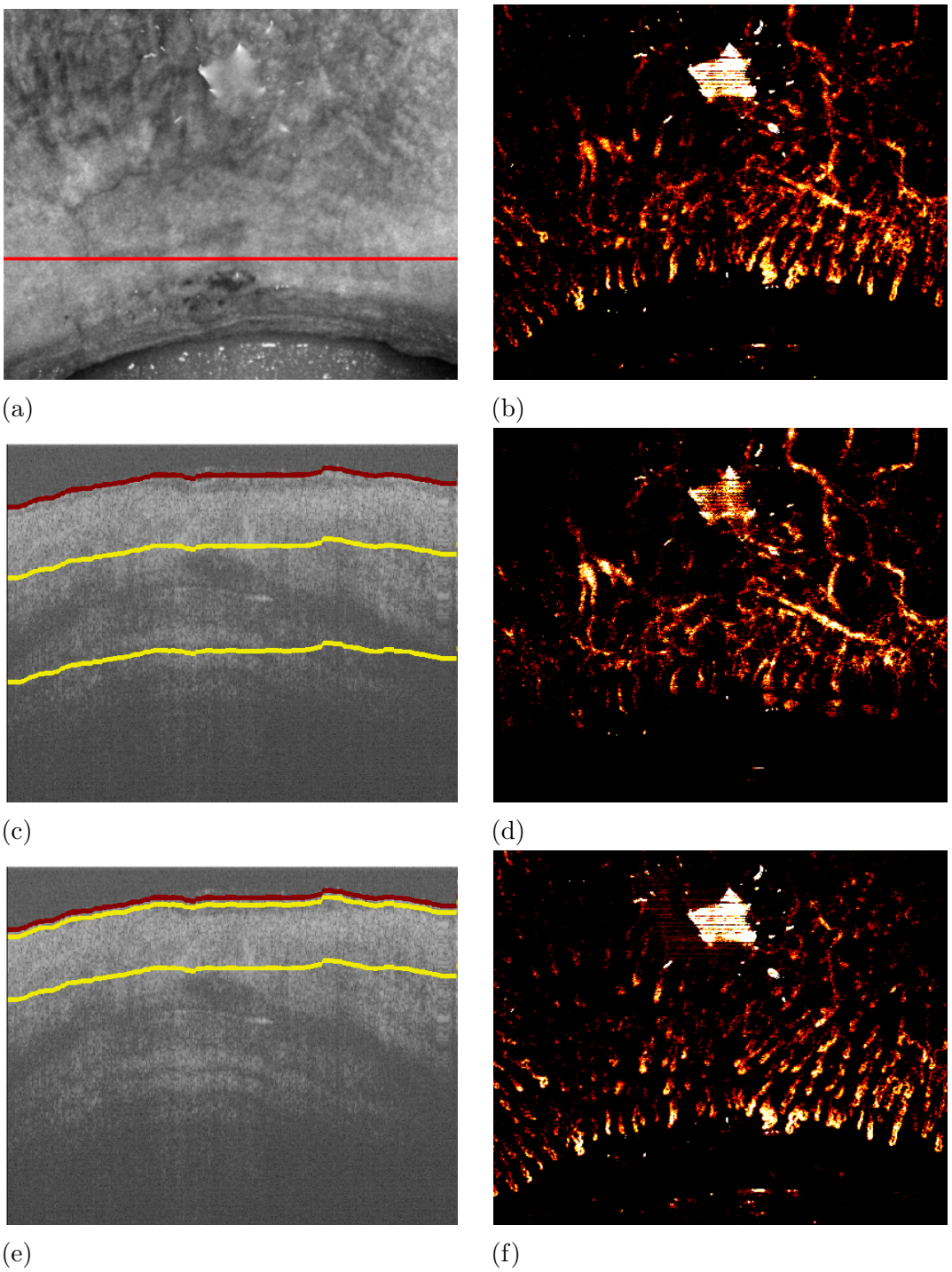

Figure 4.11: a) Surface projection, the red line indicates the location of the B-slice presented in c) and e); b) Angiography image when analysing the whole volume; c),e): structural B-scan images, the red line marks the detected surface, the yellow lines indicate the boundaries of the volume used for angiography; d), f): The resulting vessel maps when only information from a limited depth range is used. Vessels closer to the surface can be separated from deeper vessel structures. Note the typical appearance of the capillary apexes in f).

4.4.4 Reproducibility

To confirm that indeed actual vessel structures can be visualized with the system, two reproducibility experiments were performed: First, 5 subsequent measurements from the same location without intermission were taken. Second, 5 measurements from the same location but following the complete preparation procedure between the measurements were recorded.

Figure 4.12 shows the results of the immediately repeated measurements. The images vary in quality. Especially figures 4.13b, 4.13c and 4.13e clearly show artifacts originating from sample movements (horizontal lines). These movements also reduce the visibility of capillaries (most pronounced in fig. 4.13e). The undisturbed images (fig. 4.13a and fig. 4.13d) can be registered and averaged to improve image quality, this was done to produce the image shown in figure4.13f. Certain eye-catching capillaries could quite easily be distinguished in all images and were used as orientation to select the presented parts of the original images.

Figure 4.13 shows the results of five measurements taken 16 days later. After each single measurement, the sample finger was removed from the setup, cleaned from the olive oil and given a rest of about a minute. The images vary in quality. Especially figures 4.13b, 4.13c and 4.13e clearly show artifacts stemming from sample movements (horizontal lines). These movements also reduce the visibility of capillaries (most pronounced in 4.13e). The undisturbed images 4.13a and 4.13d can be registered and averaged to improve image quality, this was done to produce 4.13f. Certain eye-catching capillaries could quite easily be distinguished in all images and were used as orientation to select the presented parts of the original images.

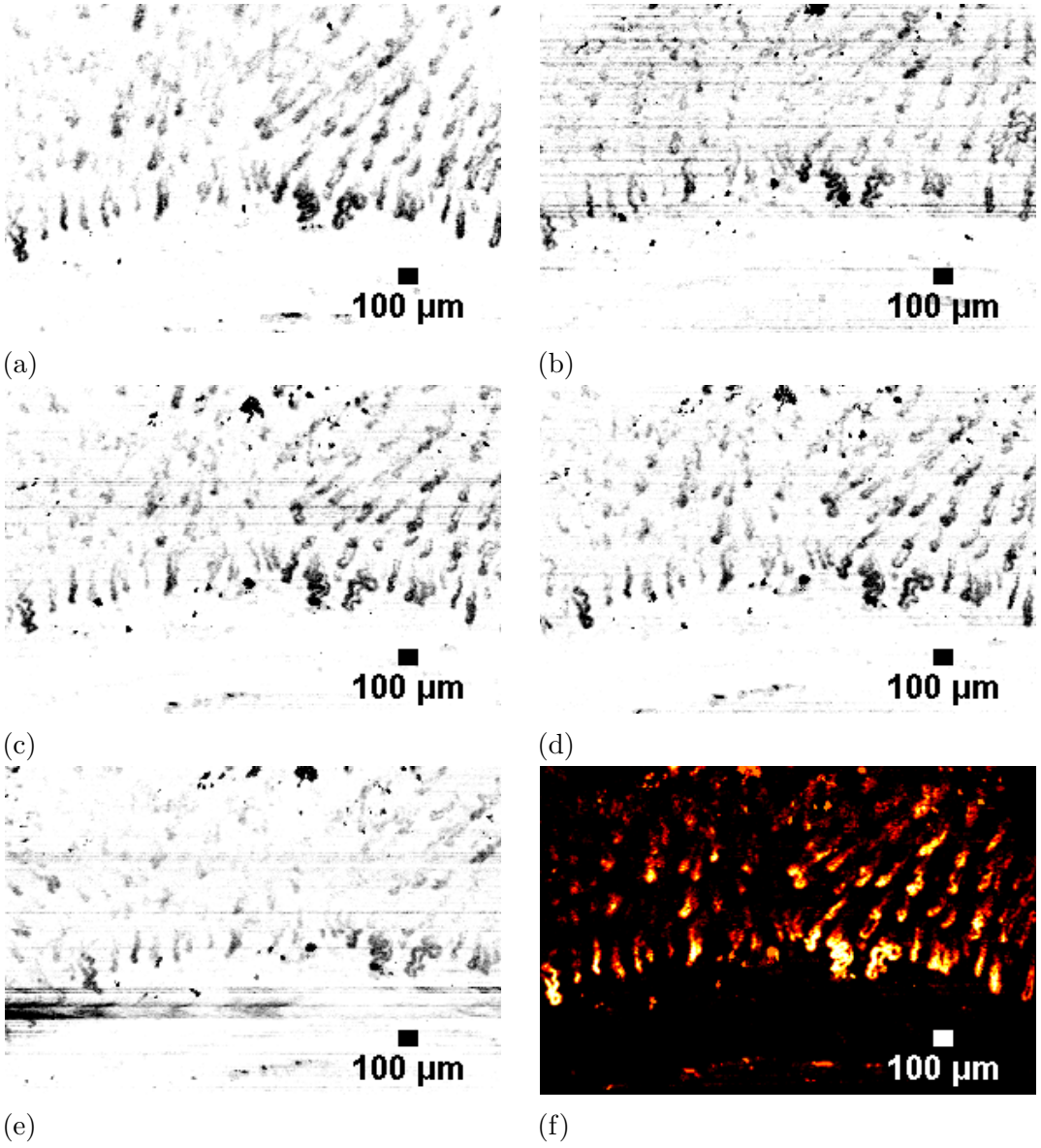

Figure 4.12: Immediately repeated measurements at the same location. Only the relevant parts of the original images are shown. a)-e) Angiography images obtained as described in section 4.4.3, f) A false-colored average of images a) and d). Note the horizontal lines originating from sample movement.

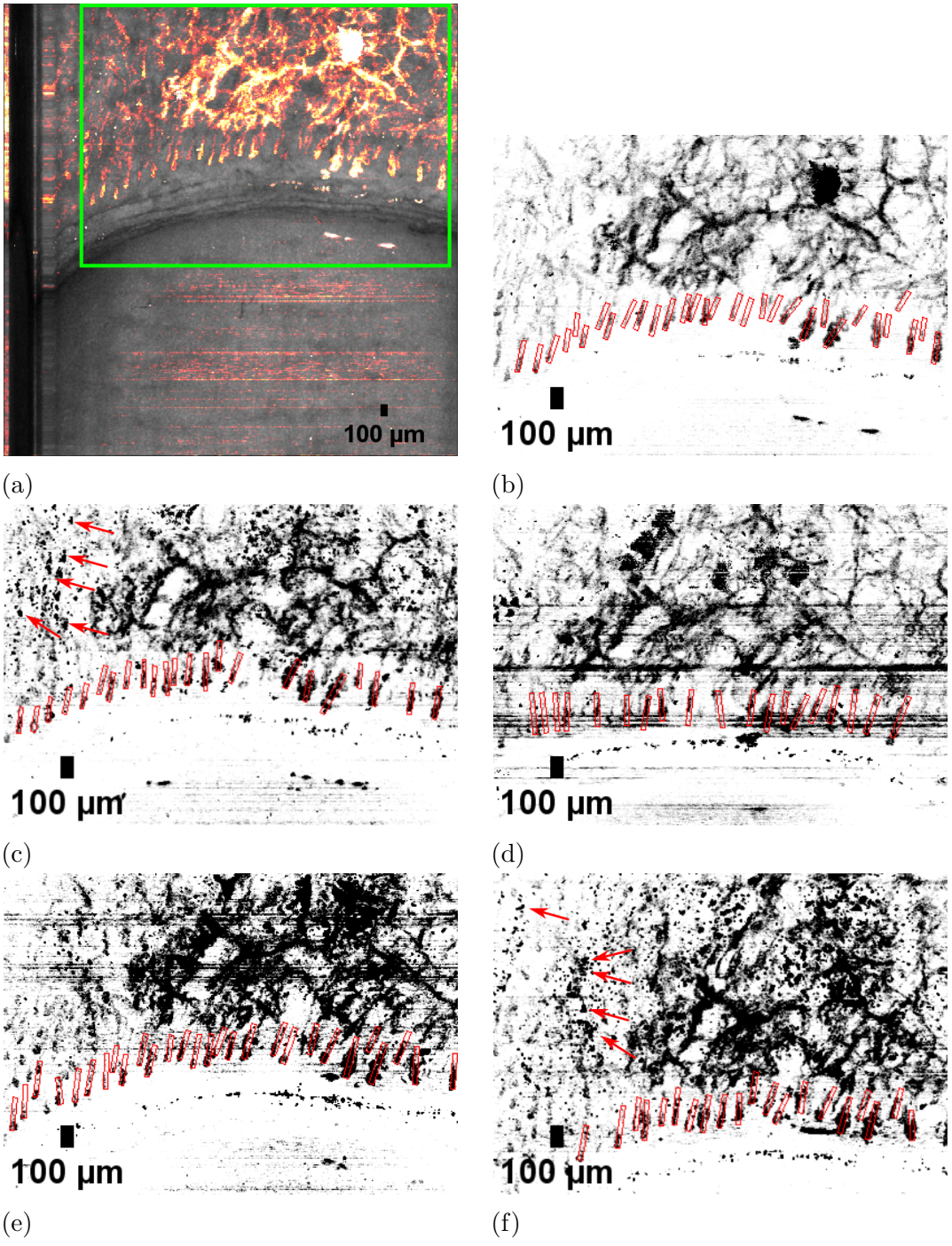

(a) (b) (c) (d) (e) (f)

Figure 4.13: Results of the second reproducibility experiment. a) Complete composite image of the first measurement, the indicated rectangle is the ROI chosen for the subsequent measurements. b)-f) Vessel maps of the pixel region indicated in a), countable capillaries are marked in all five maps. It can be seen that image quality varies rather strongly. d) and e) show motion artifacts (horizontal lines) while c) and f) show surface artifacts ("freckles" spread over the image, especially upper left corner, indicated by red arrows).

4.4.5 Functional capillary density (FCD)

Capillary microscopy and nailfold videocapillaroscopy are being evaluated for clinical use ([28], [29], [30]). It was shown that functional capillary density, capillary diameter and capillary blood flow velocities can be useful indicators for diagnosis of diseases such as diabetes mellitus and metabolic syndrome. However, there is not yet a clear definition of how to measure functional capillary density (see [31]). The two most promising options are

- Counting capillary apexes and relating them to the detection *area* (given as capillaries per square millimeter [cap/mm^2]).
- Counting capillary loops in the region closest to the nailfold and relating them to the *length* of the region (given as capillaries per millimeter [cap/mm]).

Capillary loops were counted manually and distance was measured in ImageJ. The average functional capillary density (FCD) in the first experiment was 9.11 cap/mm with a standard deviation of 0.64 cap/mm. In the second reproducibility experiment, FCD was found to be 8.23 cap/mm with a standard deviation of 1.07 cap/mm. Tables 4.1 and 4.2 show the results obtained from the images presented in 4.12 and 4.13, respectively. Further, the results are compared in figure **??**.

4.4.6 Comparison to capillaroscopy

To compare our results with the more established technique of capillaroscopy, a simple video capillaroscopy setup was constructed in a previous work ([17]). Results from that study and from literature ([32]) are shown alongside our new results in figure 4.15.

Figure 4.15a shows an even spread of visible capillary apexes over the whole image, not just a single line of capillary loops in the region nearest to the nailfold. The same holds true for the OCT vessel map in figure 4.15c, hinting that we image the same structures.

Table 4.1: Functional capillary density (FCD) measured in the 5 ROIs shown in figure 4.12.

	loops	length [mm]	FCD [cap/mm]
Image 1	22	2.34	9.40
Image 2	19	2.27	8.37
Image 3	21	2.25	9.33
Image 4	22	2.22	9.91
Image 5	17	1.99	8.54

Table 4.2: Functional capillary density (FCD) measured in the 5 ROIs shown in figure 4.13.

	loops	length [mm]	FCD [cap/mm]
Image 1	30	3.13	9.58
Image 2	23	3.13	7.35
Image 3	19	2.70	7.04
Image 4	27	3.00	9.00
Image 5	20	2.33	8.20

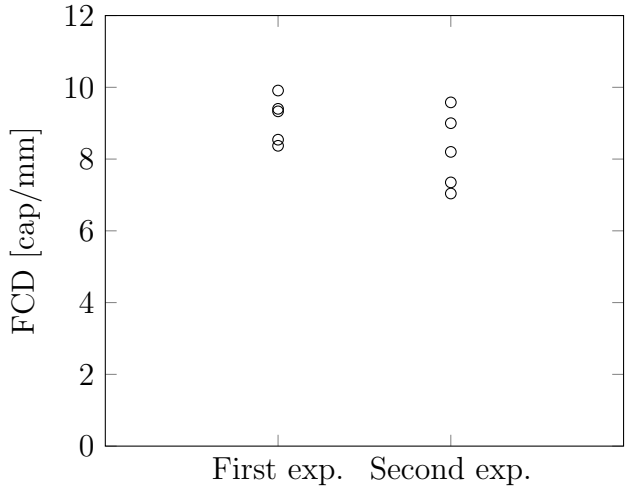

Figure 4.14: Functional capillary density scores for the two reproducibility experiments. In the second experiment (where more manipulations took place between repetitions), the FCD score is spread wider and its average is lower.

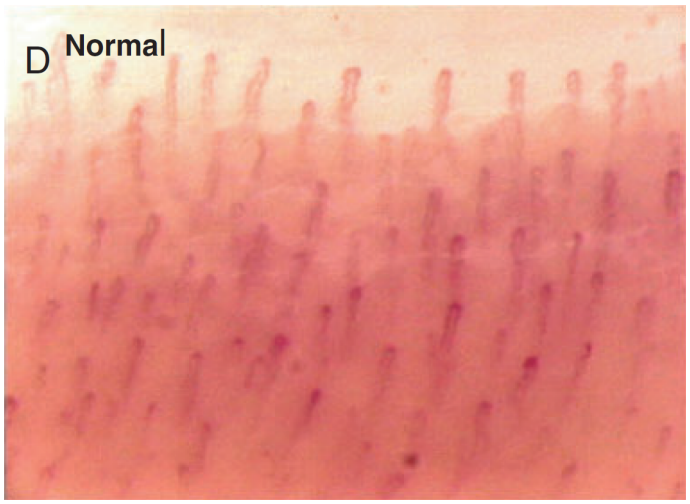

(a)

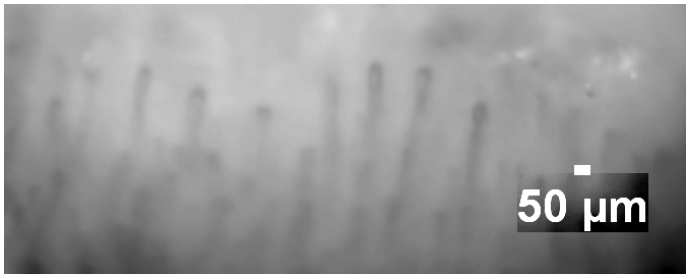

(b)

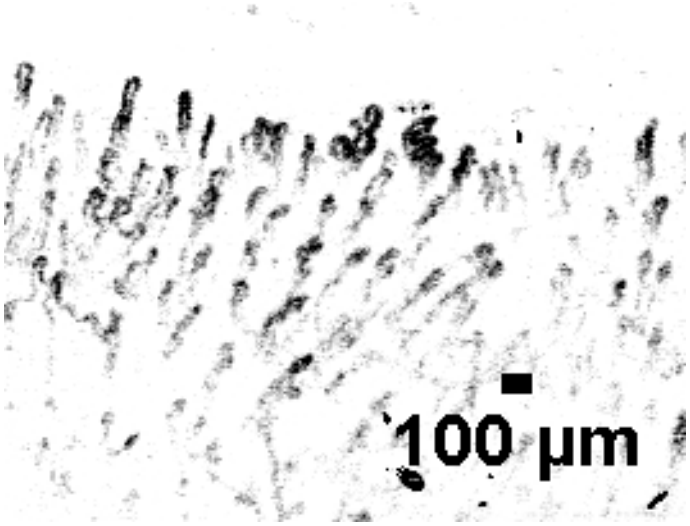

(c)

Figure 4.15: Comparison of capillary microscopy to OCT angiography images. a) Videocapillaroscopy image of a healthy subject, as found in literature. b) Videocapillaroscopy image as presented in [17]. c) OCT image taken as described in section 4.4.3, cropped and rotated to match a). Image 4.15a is reused from [32] with permission from Oxford University Press, license number 3961941134474. In the original publication, it appears as figure 1D to illustrate a normal, healthy capillary pattern (hence the label in the upper left corner).

Chapter 5

Discussion and Outlook

5.1 Discussion

In this thesis, a Fourier-Domain OCT system was adapted and used to perform in-vivo measurements on human skin.

The system provides a good signal-to-noise-ratio of 116 dB that is close to the shot-noise-limit. This results in structural images that allow discrimination of different skin layers.

It was successfully demonstrated that the system is capable of detecting vessels in the nailfold. The detected structures are in line with anatomical considerations and can be reproduced, it is therefore plausible to assume that it is indeed vessels that are shown.

The calculated functional capillary density of about $8 - 9\,\mathrm{cap/mm}$ is in accordance with published values of $9.1 - 11.8\,\mathrm{cap/mm}$ ([29]). However, there were also higher values reported such as 20.4 ± 6.5 ([28]). This might be a hint that our system does not yet detect *all* capillaries, which might be due to an insufficient sensitivity to slow flow speeds. The algorithm requires a change in the signal intensity between successive B-scans which is not the case for very slow flow speeds.

Comparing the OCT images to classic capillary microscopy images, the most striking feature is the improved contrast. Further, OCT provides information about the 3D structure of the capillary network. This is due to the higher penetration depth of the infrared light and primarily to the nature of OCT as an imaging modality that records volumetric datasets. The biggest disadvantage of the OCT approach is probably its high cost when compared to capillaroscopy. With improved automated post-processing, the OCT might reduce the need for a trained physician to evaluate capillaroscopic images, thereby improving OCT's competitiveness.

5.2 Outlook

The system was demonstrated to provide reproducible vessel maps of the human nailfold region. Further interesting experiments could involve treating the nailfold

with e.g. temperature changes prior to imaging. Supposedly, the capillaries might dilate when temperature is increased and constrict when temperature is decreased. Whether this effect is observable with the OCT system is up to question.

Further improvement of the OCT system could be achieved by using a polarized light source. By illuminating the sample with polarized light and restricting detection of light with the same polarization state, static tissue signal should be reduced and vessel signal increased.

To enable a broader clinical use, a more flexible sample arm is desirable. Possible options include a handheld design, which could enable skin imaging in most parts of the body. Making the system fit for patient use is also a necessary step towards the most natural next step: Imaging pathological vasculatures.

Slight modifications of the setup and the software would also allow for a full-range OCT protocol (see [33] and [34]). Such a configuration would allow for a larger imaging depth range and possibly also for a higher image contrast in the depth region of interest.

The post-processing software could also be expanded to automatically detect vessel structures such as capillary loops. This would be the main step to automatically calculate physiological parameters such as the Functional Capillary Density.

Another interesting endeavour would be to use the graphics processing unit (GPU) of a PC for the post-processing of the OCT data. Modern GPUs offer thousands of cores that can be used in parallel. Since the post-processing of Fourier-Domain OCT data involves a large number of parallelizable Fourier-Transforms, this might enable much faster analysis. Combined with a more economic way of generating the vessel map, this could allow for live screening of the human nailfold capillaries, turning OCT into a modern version of videocapillaroscopy.

List of Figures

Bibliography

[1] M. Cutolo, A. Sulli, and V. Smith, "How to perform and interpret capillaroscopy," *Best Practice & Research Clinical Rheumatology*, vol. 27, pp. 237–248, apr 2013.

[2] W. J. Choi, H. Wang, and R. K. Wang, "Optical coherence tomography microangiography for monitoring the response of vascular perfusion to external pressure on human skin tissue," *J. Biomed. Opt*, vol. 19, p. 056003, may 2014.

[3] Z. A. Awan, T. Wester, and K. Kvernebo, "Human microvascular imaging: a review of skin and tongue videomicroscopy techniques and analysing variables," *Clinical Physiology and Functional Imaging*, vol. 30, pp. 79–88, mar 2010.

[4] O. Gilje, "Capillary microscopic examination in skin diseases," *Archives of Dermatology*, vol. 68, p. 136, aug 1953.

[5] B. Fagrell, "The skin microcirculation and the pathogenesis of ischaemic necrosis and gangrene," *Scandinavian Journal of Clinical and Laboratory Investigation*, vol. 37, pp. 473–476, jan 1977.

[6] A. Bollinger, K. Jager, F. Sgier, and J. Seglias, "Fluorescence microlymphography," *Circulation*, vol. 64, pp. 1195–1200, dec 1981.

[7] A. Bollinger, "Pathophysiologie des raynaud-phnomens," *DMW - Deutsche Medizinische Wochenschrift*, vol. 107, pp. 1699–1701, nov 1982.

[8] R. G. Nadeau, W. Groner, J. W. Winkelman, A. G. Harris, C. Ince, G. J. Bouma, and K. Messmer, "Orthogonal polarization spectral imaging: a new method for study of the microcirculation.," *Nature Medicine*, vol. 5, pp. 1209–1212, oct 1999.

[9] C. Mørk, K. Kvernebo, C. L. Asker, and E. G. Salerud, "Reduced skin capillary density during attacks of erythromelalgia implies arteriovenous shunting as pathogenetic mechanism," *Journal of Investigative Dermatology*, vol. 119, pp. 949–953, oct 2002.

[10] J. Fujimoto and E. Swanson, "The development, commercialization, and impact of optical coherence tomography," *Investigative Opthalmology & Visual Science*, vol. 57, p. OCT1, jul 2016.

[11] A. F. Fercher, K. Mengedoht, and W. Werner, "Eye-length measurement by interferometry with partially coherent light," *Optics Letters*, vol. 13, p. 186, mar 1988.

[12] D. Huang, E. Swanson, C. Lin, J. Schuman, W. Stinson, W. Chang, M. Hee, T. Flotte, K. Gregory, C. Puliafito, and J. Fujimoto, "Optical coherence tomography," *Science*, vol. 254, pp. 1178–1181, 1991.

[13] A. F. Fercher, C. K. Hitzenberger, W. Drexler, G. Kamp, and H. Sattmann, "In vivo optical coherence tomography," *American Journal of Ophthalmology*, vol. 116, pp. 113–114, jul 1993.

[14] R. Leitgeb, C. Hitzenberger, and A. Fercher, "Performance of fourier domain vs time domain optical coherence tomography," *Optics Express*, vol. 11, p. 889, apr 2003.

[15] L. An, J. Qin, and R. K. Wang, "Ultrahigh sensitive optical microangiography for in vivo imaging of microcirculations within human skin tissue beds," *Optics Express*, vol. 18, p. 8220, apr 2010.

[16] J. Xu, W. Wei, S. Song, X. Qi, and R. K. Wang, "Spectral-domain optical coherence tomography-based angiography for scalable wide-field vascular imaging," in *Biomedical Optics 2016*, The Optical Society, 2016.

[17] M. E. Fürst, "Polarization sensitive capillary microscopy." Project Work, Technical University of Vienna, 2016.

[18] O. Sander, C. Sunderkötter, I. Kötter, I. Wagner, M. Becker, I. Herrgott, A. Schwarting, B. Ostendorf, C. Iking-Konert, and E. Genth, "Kapillarmikroskopie," *Z. Rheumatol.*, vol. 69, pp. 253–262, mar 2010.

[19] A. F. Fercher, "Optical coherence tomography," *Journal of Biomedical Optics*, vol. 1, no. 2, p. 157, 1996.

[20] A. G. Podoleanu, "Optical coherence tomography," *The British Journal of Radiology*, vol. 78, pp. 976–988, nov 2005.

[21] W. Demtröder, *Experimentalphysik 2*. Springer Berlin Heidelberg, 2009.

[22] M. Choma, M. Sarunic, C. Yang, and J. Izatt, "Sensitivity advantage of swept source and fourier domain optical coherence tomography," *Opt. Express*, vol. 11, p. 2183, sep 2003.

[23] J. F. de Boer, B. Cense, B. H. Park, M. C. Pierce, G. J. Tearney, and B. E. Bouma, "Improved signal-to-noise ratio in spectral-domain compared with time-domain optical coherence tomography," *Optics Letters*, vol. 28, p. 2067, nov 2003.

[24] S. Yousefi, Z. Zhi, and R. K. Wang, "Eigendecomposition-based clutter filtering technique for optical microangiography," *IEEE Transactions on Biomedical Engineering*, vol. 58, pp. 2316–2323, aug 2011.

[25] B. J. Vakoc, S. H. Yun, J. F. de Boer, G. J. Tearney, and B. E. Bouma, "Phase-resolved optical frequency domain imaging," *Opt. Express*, vol. 13, no. 14, p. 5483, 2005.

[26] H. M. Subhash, V. Davila, H. Sun, A. T. Nguyen-Huynh, X. Shi, A. L. Nuttall, and R. K. Wang, "Volumetric in vivo imaging of microvascular perfusion within the intact cochlea in mice using ultra-high sensitive optical microangiography," *IEEE Transactions on Medical Imaging*, vol. 30, pp. 224–230, feb 2011.

[27] Z. Hu, Y. Pan, and A. M. Rollins, "Analytical model of spectrometer-based two-beam spectral interferometry," *Applied Optics*, vol. 46, p. 8499, dec 2007.

[28] P. A. Maranhão, M. das Graças Coelho de Souza, L. G. Kraemer-Aguiar, and E. Bouskela, "Dynamic nailfold videocapillaroscopy may be used for early detection of microvascular dysfunction in obesity," *Microvascular Research*, vol. 106, pp. 31–35, jul 2016.

[29] L. G. Kraemer-Aguiar, C. M. Laflor, and E. Bouskela, "Skin microcirculatory dysfunction is already present in normoglycemic subjects with metabolic syndrome," *Metabolism*, vol. 57, pp. 1740–1746, dec 2008.

[30] L. G. K. de Aguiar, C. M. Laflor, L. Bahia, N. R. Villela, N. Wiernsperger, D. A. Bottino, and E. Bouskela, "Metformin improves skin capillary reactivity in normoglycaemic subjects with the metabolic syndrome," *Diabetic Medicine*, vol. 24, pp. 272–279, mar 2007.

[31] T. Klyscz, M. Jünger, F. Jung, and H. Zeintl, "Cap image - ein neuartiges computeruntersttztes videobildanalysesystem fr die dynamische kapillarmikroskopie - cap image - a newly-developed computer-aided videoframe analysis system for dynamic capillaroscopy," *Biomedizinische Technik/Biomedical Engineering*, vol. 42, no. 6, pp. 168–175, 1997.

[32] M. Cutolo, "Nailfold capillaroscopy is useful for the diagnosis and follow-up of autoimmune rheumatic diseases. a future tool for the analysis of microvascular heart involvement?," *Rheumatology*, vol. 45, pp. iv43–iv46, oct 2006.

[33] B. Baumann, M. Pircher, E. Gtzinger, and C. K. Hitzenberger, "Full range complex spectral domain optical coherence tomography without additional phase shifters," *Opt. Express*, vol. 15, no. 20, p. 13375, 2007.

[34] J. Jungwirth, B. Baumann, M. Pircher, E. Gotzinger, and C. K. Hitzenberger, "Extended in vivo anterior eye-segment imaging with full-range complex spectral domain optical coherence tomography," *J. Biomed. Opt.*, vol. 14, no. 5, p. 050501, 2009.